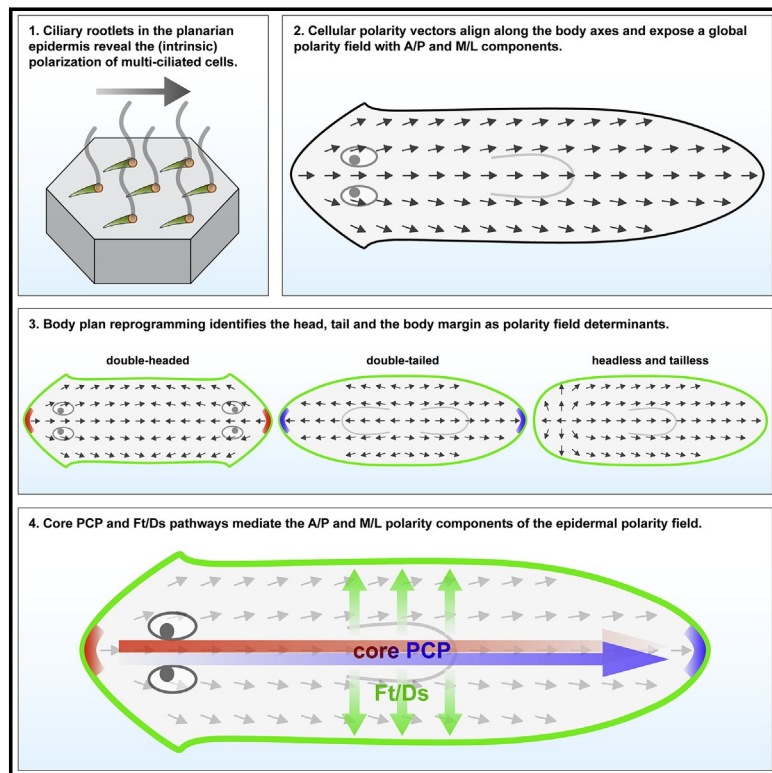


Developmental Cell

Dynamic Polarization of the Multiciliated Planarian Epidermis between Body Plan Landmarks

Graphical Abstract



Authors

Hanh Thi-Kim Vu, Sarah Mansour, Michael Kücke, ..., Eugene Wimberly Myers, Lutz Brusch, Jochen Christian Rink

Correspondence

lutz.brusch@tu-dresden.de (L.B.), rink@mpi-cbg.de (J.C.R.)

In Brief

Ciliary rootlets in the planarian epidermis are globally polarized. Head, tail, and body margin orient the polarity field, which can be modeled by the superposition of independent A/P and M/L polarity components. Vu et al. identify core PCP and Ft/Ds pathways as mediators of the A/P and M/L polarization components.

Highlights

- The multi-ciliated planarian epidermis is polarized along the A/P and M/L body axes
- Head, tail, and body margin dynamically determines the epidermal polarity field
- Core PCP mediates the A/P polarization component
- Ft/Ds mediates the M/L polarization component



Dynamic Polarization of the Multiciliated Planarian Epidermis between Body Plan Landmarks

Hanh Thi-Kim Vu,^{1,6} Sarah Mansour,^{1,6} Michael Kücken,² Corinna Blasse,¹ Cyril Basquin,³ Juliette Azimzadeh,³ Eugene Wimberly Myers,^{1,4} Lutz Brusch,^{2,*} and Jochen Christian Rink^{1,5,7,*}

¹Max Planck Institute for Molecular Cell Biology and Genetics, Pfotenhauerstrasse 108, 01307 Dresden, Germany

²Technische Universität Dresden, Zentrum für Informationsdienste und Hochleistungsrechnen (ZIH), Helmholtzstrasse 10, 01069 Dresden, Germany

³Institut Jacques Monod, Bâtiment Buffon, 15 rue Hélène Brion, 75205 Paris CEDEX 13, France

⁴Center for Systems Biology Dresden, Pfotenhauerstrasse 108, 01307 Dresden, Germany

⁵Max Planck Institute for Biophysical Chemistry, Am Fassberg 11, 37077 Göttingen, Germany

⁶These authors contributed equally

⁷Lead Contact

*Correspondence: lutz.brusch@tu-dresden.de (L.B.), rink@mpi-cbg.de (J.C.R.)

<https://doi.org/10.1016/j.devcel.2019.10.022>

SUMMARY

Polarity is a universal design principle of biological systems that manifests at all organizational scales, yet its coordination across scales remains poorly understood. Here, we make use of the extreme anatomical plasticity of planarian flatworms to probe the interplay between global body plan polarity and local cell polarity. Our quantitative analysis of ciliary rootlet orientation in the epidermis reveals a dynamic polarity field with head and tail as independent determinants of anteroposterior (A/P) polarization and the body margin as determinant of mediolateral (M/L) polarization. Mathematical modeling rationalizes the global polarity field and its response to experimental manipulations as superposition of separate A/P and M/L fields, and we identify the core PCP and Ft/Ds pathways as their molecular mediators. Overall, our study establishes a framework for the alignment of cellular polarity vectors relative to planarian body plan landmarks and establishes the core PCP and Ft/Ds pathways as evolutionarily conserved 2D-polarization module.

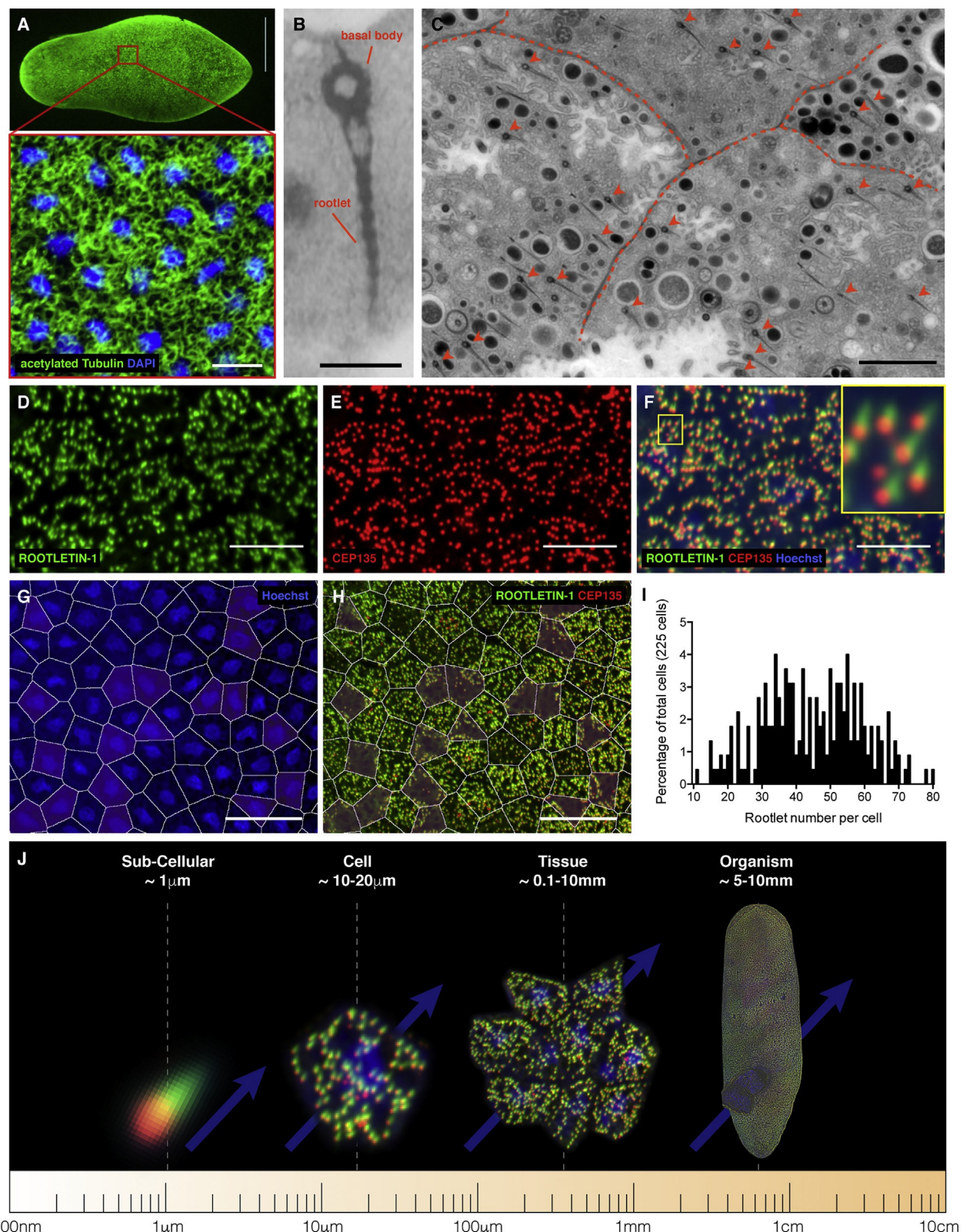
INTRODUCTION

Polarity is a fundamental design principle of biological systems that manifests as the end-to-end polarity of cytoskeletal fibers, the polarized distribution of proteins within cells or across tissues or the opposite location of head and tail at the organismal level. Yet the invariant head-tail alignment of scales in the fish skin, of cilia in the *Xenopus* larval epidermis or the wing hair polarity fields in the fruit fly wing demonstrate the coordination of polarity vectors across scales. How this can be achieved remains a fascinating problem.

Polarity is best understood at the cell and tissue levels. Here, we focus on the evolutionarily conserved core planar cell polarity (PCP) pathway that polarizes cells along the plane of the tissue (Adler, 2012; Butler and Wallingford, 2017; Hale and Strutt, 2015; Yang and Mlodzik, 2015). Pathway components include transmembrane proteins such as Frizzled (Fz), Van Gogh (Vang) and Flamingo (Fmi), intracellular proteins Disheveled (Dvl), Diego (Dgo) and Prickle (Pk) and additional effectors. Mutual antagonism between two subcomplexes, the Fz/Dvl/Dgo complex and the Vang/Pk complex, establishes a cell-intrinsic polarity vector between Fz/Dvl or Vang/Pk membrane domains. The interaction between Fz/Fmi dimers of one cell and the Vang/Fmi dimers of its neighbor results in the emergence of ordered tissue-scale PCP-polarity fields. A parallel pathway involving the atypical cadherins Fat (Ft) and Dachsous (Ds) and the intracellular components Dachs and Four-jointed (Fj) establishes cell and tissue polarity in a conceptually similar manner. These two pathways variously interact during fly-wing development (Goodrich and Strutt, 2011; Lawrence et al., 2007; Matis and Axelrod, 2013; Merkel et al., 2014). Interactions between junctional polarity complexes and the cytoskeleton ultimately mediate wing-hair alignment in *Drosophila* or the axial alignment of cilia in the multiciliated cells (MCC) of vertebrates (Butler and Wallingford, 2017). While current cell culture and developmental model systems offer experimental access to polarity emergence and cell-cell coordination, the global coordination of polarity remains more difficult to address.

Ideally, a model system for the global coordination of polarity should allow the manipulation of organismal body plan polarity. While this is difficult to achieve in developing embryos, planarian flatworms offer a model system in which such manipulations are uniquely possible. RNA interference (RNAi) against Wnt pathway components in adult worms can induce the rapid conversion of the tail into a head or the sprouting of ectopic heads all along the body margins (Gurley et al., 2008; Iglesias et al., 2008; Petersen and Reddien, 2008). In conjunction with their formidable regenerative powers, RNAi can further induce the formation of a tail instead of a head and vice versa or the regeneration



**Figure 1. Ciliary Rootlets as Polarity Indicators**

(A) Whole-mount staining (anti-acetylated tubulin) of the densely ciliated ventral epidermis. Scale bar: 500 μ m. Zoomed view: axonemes (green) and epidermal nuclei (DAPI, blue). Scale bar: 10 μ m.

of tissue devoid of head or tail identity (Blassberg et al., 2013; Chen et al., 2013). In addition to a reprogrammable adult body plan, the cilia-driven gliding motility of planarians strongly hints at globally coordinated PCP. The ventral epidermis is largely comprised of MCC (Glazer et al., 2010; Rink et al., 2009; Rompolas et al., 2013). Cilia-driven transport generally requires the rotational polarization of cilia within individual MCC and the planar coordination of rotational polarity vectors at the tissue scale (Butler and Wallingford, 2017). Both can be visualized via the alignment of ciliary rootlets, an evolutionarily conserved macromolecular complex that anchors the ciliary axoneme to the cytoskeleton (Frisch and Farbman, 1968; Park et al., 2008; Yang et al., 2002). With adult body plan polarity as an experimental variable and ciliary rootlet orientation as putative readout of cell- and tissue-scale polarity, planarians therefore promise unique access to the coordination of polarity between the organismal and cellular scales.

We here describe a seminal analysis of ciliary rootlet orientation within the epidermis of the planarian model species *S. mediterranea* (Smed). Through experiments and mathematical modeling, we find that the head tip, tail tip, and body edge act as collective determinants of a global epidermal polarity field. Further, we identify the core PCP and Ft/Ds pathways as specific mediators of rootlet polarization along the A/P and M/L body axes. Overall, our study establishes a framework for the alignment of cellular polarity vectors with the landmarks of the planarian body and a new model system for probing the multiscale coordination of polarity.

RESULTS

Ciliary Rootlets as Epidermal Polarity Indicators

The ventral planarian epidermis is comprised of regularly spaced MCC, with their protruding axonemes forming a dense lawn of cilia (Figure 1A). While polarity cannot be inferred from the axonemes (Figure 1A), the macromolecular rootlet that anchors each axoneme within the cell cortex is often aligned with the direction of the ciliary beat (Frisch and Farbman, 1968; Park et al., 2008; Rieger, 1981; Yang et al., 2002). Electron micrographs of the Smed ventral epidermis revealed striated rootlets and a basal foot projecting in the opposite direction from the basal body (Figure 1B). Grazing sections further demonstrated the parallel alignment of rootlets within and between epidermal cells (Figure 1C), thus establishing the principal utility of rootlet orientation as experimental readout for rotational and planar cell polarity in Smed.

Faced with the need to visualize micron-length rootlets across centimeter-long worms, we turned to light microscopy. We used an antibody against the basal body component SMED-CEP135

(Azimzadeh et al., 2012) and additionally raised a monoclonal antibody against SMED-ROOTLETIN-1, one of the two Smed homologues of the conserved *rootletin* gene (Figures S1A and S1B) and the major structural constituent of rootlets (Yang et al., 2002). Both antibodies labeled abundant structures in ventral epidermal cells (Figures 1D and 1E) that resolve into dot-like CEP135-positive centrosomes at the broad end of chevron-shaped ROOTLETIN-1-positive rootlets (Figure 1F). The regularly spaced MCC further have a diameter of ~10–15 μ m in (Figures 1G, 1H, and S1D–S1F) and harbor an average of approximately 40 rootlets/cell (Figure 1I). At least some of the interspersed cells with few or no cilia that we observe (Figure 1H) likely represent postmitotic progenitors integrating from deeper tissue layers (Tu et al., 2015; van Wolfswinkel et al., 2014), which highlights the intrinsically dynamic nature of the Smed epidermis (see Discussion). We further developed an imaging pipeline comprising tiled z stack volume acquisition on a spinning disk confocal microscope, automated stitching of the resulting image stacks, epidermal layer extraction, rootlet detection, and directionality quantification (Figure S1C, (Blaesse et al., 2017)). Verification with manually annotated ground truth data confirmed both the sensitivity and accuracy of our rootlet analysis pipeline (Figures S1G–S1L). Overall, these tools provide a toolkit for the multiscale analysis of polarity within the Smed epidermis (Figure 1J), as previously demonstrated in *Xenopus* larval skin (Park et al., 2008).

Polarity Field of the Ventral Epidermis

Organismal body plan polarity in Smed is revealed by the position of the eyes in the head and specific gene expression domains (Figure 2A). To probe tissue and cell scale polarity, we quantified rootlet orientation across the entire ventral epidermis (Figure 2B). Local rootlet orientation averaging within 100- μ m squares (~80 cells/3000 rootlets) and plotting the resulting vector for each square revealed that rootlets predominantly orient along the A/P axis (Figure 2C), consistent with cilia-driven gliding. Further, especially in the head region, average rootlet orientation vectors deviated toward the body margins (referred to as “splay” below). The evident long-range coordination of local polarity vectors reveals the orientation of MCC rootlets relative to body plan landmarks, much like wing hairs in *Drosophila* (Adler, 2012) or cilia in vertebrate multiciliated epithelia (Butler and Wallingford, 2017).

We next took advantage of the large number of rootlet quantifications (~1–2 million rootlets/animal) and our pipeline’s processing capacity (typically six whole mount animals/condition) to quantify Smed epidermal polarization. To assess the spatial coherence of rootlet orientation, we analyzed the auto-correlation of average cilia orientation within 150 \times 150 pixel

(B) TEM image of a longitudinally sectioned ciliary rootlet. Scale bar: 500 nm.

(C) TEM image of a grazing section of the ventral epidermis: dashed lines, cell-cell boundaries; arrowheads, ciliary rootlets. Scale bar: 2.2 μ m.

(D–F) Rootlet visualization by confocal microscopy. Anti-SMED-ROOTLETIN-1 (D) and anti-SMED-CEP135 (E) staining, overlaid with nuclear staining (Hoechst) in the merge (F). Zoomed view: chevron-shaped ROOTLETIN signal and offset basal body staining as polarity indicators. Scale bar: 10 μ m.

(G) Computational cell boundary approximation by Voronoi tessellation (white outlines) of nuclei (DAPI, blue).

(H) Anti-ROOTLETIN-1 (green) and anti-CEP135 (red) staining of the same cell field as in (G), illustrating good agreement between actual and inferred cell outlines. Non-ciliated small cells (purple overlay) largely account for discrepancies. Scale bar: 25 μ m.

(I) Manual quantification of rootlet numbers per cell, (n = 225 cells from six wild-type specimens). Cell boundary inference as in G.

(J) Multiscale polarity analysis afforded by our analysis pipelines.

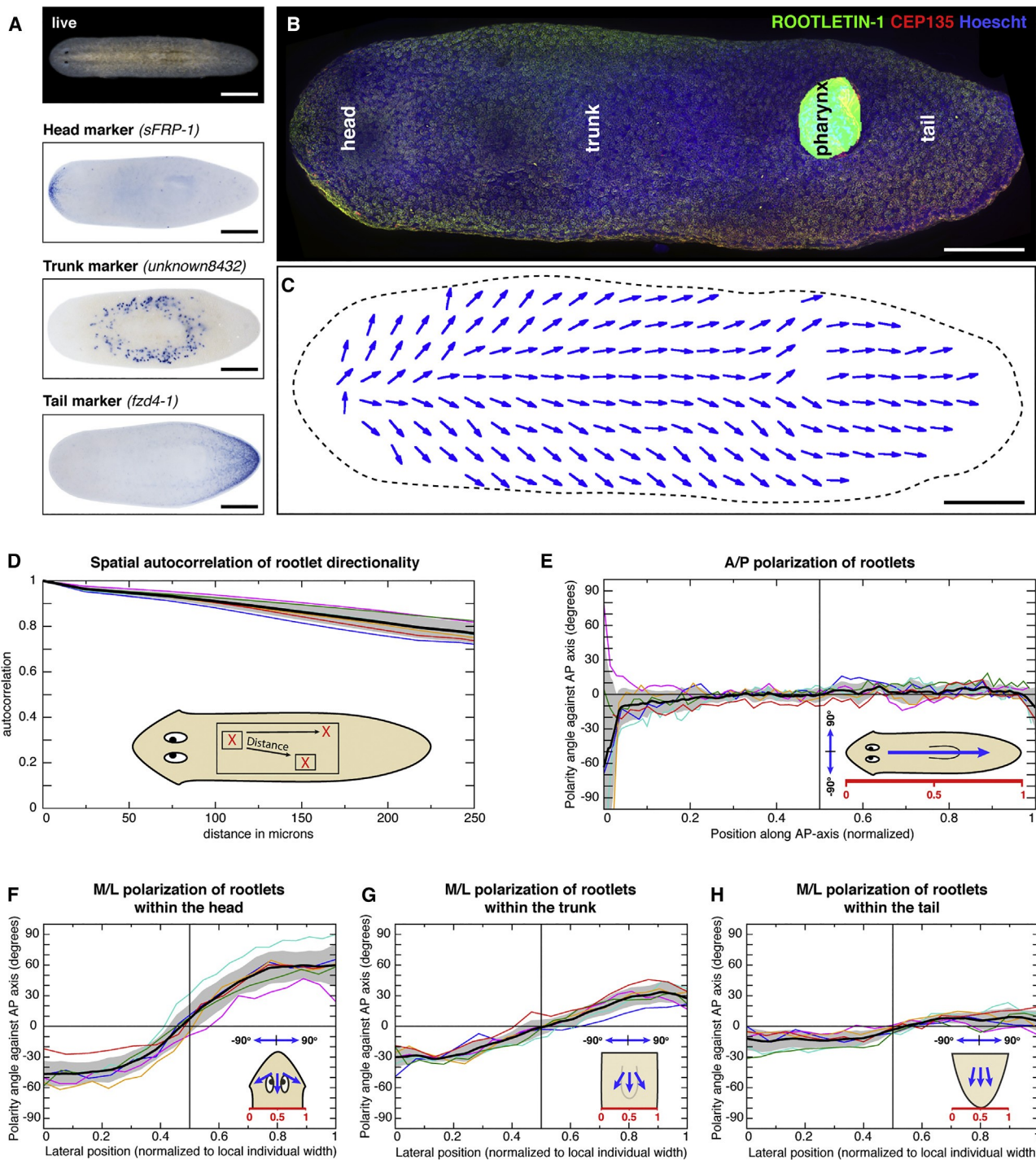


Figure 2. Polarity Field of the Ventral Epidermis

(A) Smed anatomical polarity. Live image (top), whole mount *in situ* hybridization gene expression patterns of indicated marker genes (bottom). Scale bar: 500 μ m.

(B) Tiled surface extraction of wild type Smed ventral epidermis. Antibody staining as indicated, nuclear labeling with Hoechst (blue). Scale bar: 250 μ m.

(C) Vector field representation of rootlet orientation in (B). Arrows point along the centrosome-rootlet vector. Scale bar: 250 μ m.

(D) Spatial autocorrelation of rootlet orientation, assaying directional coherence within squares of 150 \times 150 pixels as a function of distance (μ m).

(E) Rootlet A/P polarization. $n=6$ specimens; rootlet orientation was averaged orthogonal to the midline and individual traces are normalized by length. Deviations at the head and tail tip represent folding artifacts.

(legend continued on next page)

windows (~1–2 cells). The measured values remained above 80% within 200 μm (Figure 2D), which quantitatively confirms the planar polarization of MCC rotational polarity. To analyze rootlet orientation in relation to body plan polarity, we defined 0° as signifying perfect alignment with the head-tail axis, 180° as opposite tail/head orientation and 90° or 270° as orthogonal orientation to the midline. This quantitative assessment of rootlet polarization confirmed both the predominant A/P orientation (Figure 2E), but also the above-noted splay (Figures 2F–2H). In the head (Figure 2F), rootlets at the body margins orient partially toward the body edge (~ -45° left margin, 45° right margin), while rootlets in the vicinity of the planarian midline orient perfectly along the A/P axis. The highly reproducible sigmoidal shape of the M/L orientation traces further revealed that the magnitude of the splay progressively decreases along the A/P axis (Figures 2G and 2H). Overall, the orientation of individual ciliary rootles in the Smed epidermis thus reveals a globally coordinated polarity field that orients relative to both the A/P and M/L axes of the body plan.

Head, Tail, and the Body Margin as Polarity Determinants

To localize the determinants that orient the epidermal polarity field, we took advantage of Smed's anatomical plasticity. RNAi of *Smed-β-catenin-1* forces regeneration of heads instead of tails (Gurley et al., 2008; Iglesias et al., 2008; Petersen and Reddien, 2008) and can thus generate double-headed animals (Figure 3A). Intriguingly, double-headed specimens displayed bipolar polarity fields (Figures 3B and S2A–S2C). This observation identifies the head as polarity determinant that orients cell polarity away from the body margin. Further, the sharp polarity reversal at the geometric midpoint (Figure 3C) implies the propagation of the effect into the pre-existing tissue (pigmented area in Figure 3A). To interrogate putative polarizing functions of the Smed tail, we examined the double-tailed animals that regenerate from trunk pieces under *Smed-APC(RNAi)* (Figure 3D). Double-tails also displayed symmetric bipolar polarity fields (Figures 3E, 3F, and S2D–S2F), yet interestingly, with polarity vectors invariably oriented toward the body margins and thus oppositely to double-headed animals. Therefore, the tail also acts as polarity determinant and the head-tail orientation of the wild-type epidermal polarity field reflects the synergistic interplay between two global determinants. The head- and tail-less animals that result from regeneration under knockdown of *Smed-pbx* (Figure 3G) (Blassberg et al., 2013; Chen et al., 2013) provide an opportunity to assess the polarity field in the absence of both A/P polarity determinants. Remarkably, *pbx(RNAi)* animals still displayed coherent long-range polarity after 14 days of regeneration (Figures 3H and S3B). Neither the predominant A/P orientation (Figure 3G) nor the lateral splay (Figure S3C) was generally affected, thus demonstrating the maintenance of tissue polarity even in the absence of head or tail. However, *pbx(RNAi)* regenerates invariably displayed a specific reversal of tissue polarity at the “anterior” end (Figures 3I and

S3D), which would be consistent with a generally “attractive” influence of the body margin on rootlet orientation. Overall, our experiments establish head, tail, and possibly also the body margin as determinants of the epidermal polarity field in Smed.

Model Development, Parametrization, and Validation

To explore the principal sufficiency of the identified polarity determinants, we turned to mathematical modeling. Our model is inspired by the importance of compartment boundaries in fly wing polarity establishment (Sagner et al., 2012), but we deliberately take a coarse-grained approach that does not make any assumptions regarding the underlying molecular mechanisms. We make four fundamental assumptions (Figure 4A): (1) cells are intrinsically polarized; (2) head, tail, and body edge locally fix cellular polarity vectors and thus specify boundary conditions; (3) the polarity states propagate from the boundary via neighbor-neighbor coupling into the cell field; and (4) the rotational polarity of ciliary rootlets orients according to the sum of all polarity cues. Specifically, the polarity field $\vec{P}(\vec{x})$ as the model's actual representation of rootlet orientation emerges from the superposition of two independent polarity components, the A/P field \vec{A} governed by the synergistic effects of the head and tail boundary vectors, and the radially directed M/L field \vec{M} governed by the body margin. We define both fields on a two-dimensional domain approximating the planarian body shape, which renders the precise value of \vec{A} and \vec{M} a function of the spatial position $\vec{x} = (x, y)$. Mathematically, $\vec{A}(\vec{x})$ and $\vec{M}(\vec{x})$ are defined by simple linear partial differential equations with no flux boundary conditions and boundary-restricted reaction terms, the superposition of which generates the field $\vec{P}(\vec{x})$ (Figure 4B). More parsimonious models with only one polarity field can also qualitatively explain multiple features of the observed polarization patterns, but are less well supported by experimental evidence (see below and STAR Methods). Overall, our model allows the quantitative analysis of the interplay between local polarity and global determinants (Figures S4A–S4H), as well as the prediction of the dynamic consequences of experimental perturbations (Figures S4I–S4M).

We first explored the extent to which the model can reproduce the steady-state polarity field (Figure 2). A combination of analytical and numerical data-based parameter inference, using the simulation software Morpheus (Starruß et al., 2014) and pyABC for Bayesian parameter estimation (Klinger et al., 2018), recapitulated both the predominant A/P orientation, as well as the A/P graded lateral splay (Figure 4C). The latter requires restriction of the head boundary effect (H) to the head tip, which corresponds to the presumed location of the planarian head organizer (Chen et al., 2013; Oderberg et al., 2017; Vásquez-Doorman and Petersen, 2014; Vogg et al., 2014). Further, the tail needs to be more strongly polarizing than the head ($\alpha_T/\beta_T > \alpha_H/\beta_H$) in order to obtain a graded relative contribution of the M field along the A/P axis, despite the globally uniform radial polarization effect of the body margin. The quantitative recapitulation of the

(F–H). Rootlet M/L polarization in the head (F), trunk (G), and tail (H). N = 6 specimens; rootlet orientation was averaged parallel to the midline and individual traces are normalized by width.

(D–H) Colored lines: individual specimens; black lines and gray shading: mean and standard deviation (SD). 0°: head to tail orientation, +/- 90° orthogonal orientations.

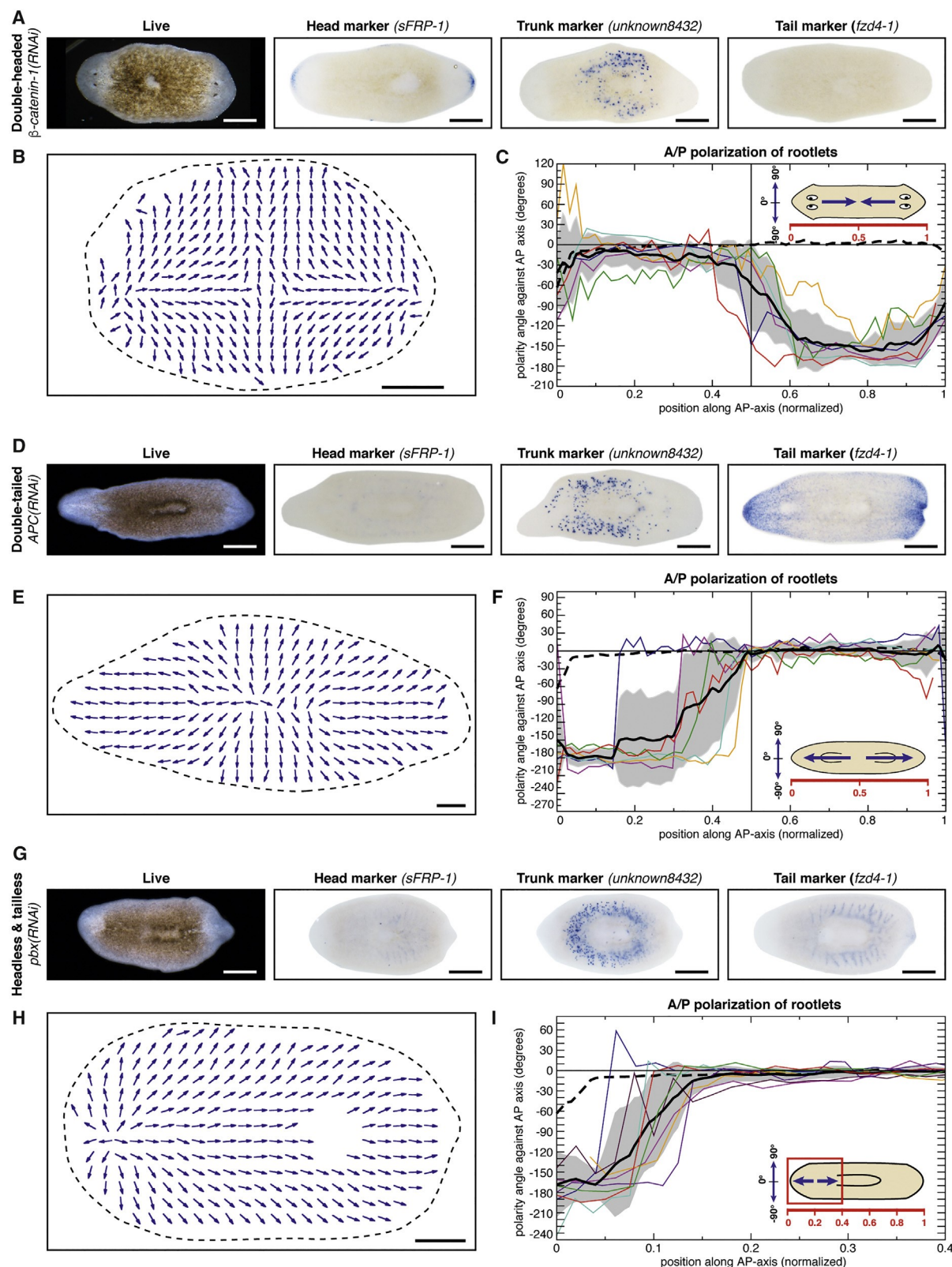


Figure 3. Epidermal Polarity Determinants

(A) Double-headed Smed regenerated from a β -catenin-1(RNAi) trunk piece. Left: Live image. Right: Head, trunk, and tail marker expression by in situ hybridization. Scale bar: 500 μ m.

measured splay profile under these conditions (Figure S4A) provides a first line of evidence for the validity of our model.

Next, we assessed the model's ability to recapitulate our previous experimental polarity field alterations (Figure 3). Solely the substitution of wild-type pole locations ($H(\vec{x})$, $T(\vec{x})$) without any additional parameter tuning was sufficient for recapitulating the symmetric bipolar polarity field of β -catenin-1(RNAi) or APC(RNAi) animals (Figures 4D and 4E). The model could also qualitatively reproduce the localized anterior polarity reversal in head- and tailless *pbx*(RNAi) animals (Figure 4F) as a dynamic intermediate state after the combined head and tail cue inactivation ($\alpha_H, \alpha_T = 0$). Despite specific differences between model predictions and experimental observations (see Discussion), this result provides additional evidence for the polarity-determining role of the body margin.

To further test the predictive utility of our model, we examined the dynamic transformation of the unidirectional steady-state polarity field into the symmetric bipolar state of double heads (Figure 3A). Rootlet orientation quantifications in β -catenin-1(RNAi) regeneration time course experiments revealed that the polarity reversal initiates at the future ectopic head tip between 3 and 4 days of regeneration and then progresses into the pre-existing tissue in a front-like manner (Figures 4G, 4H, and S4I–S4M). Quantitatively, the speed of front progression gradually slows over time (Figure 4H). While these observations raise multiple questions (see Discussion), they also conform qualitatively to a simulated change in the boundary state and its ensuing propagation by neighbor–neighbor coupling (Video S1). To further probe the quantitative agreement between model and experiment, we fixed the universal time unit of all model parameters at 1 h while keeping all other parameters unchanged from the previously determined best fit to the wild-type steady state (Figures 4C and S4A). Interestingly, the resulting simulated $x_F(t)$ trajectory (Figure 4I, black line) not just recapitulates the initial three-day lag, but also the gradual slowdown of the repolarization front during the approach to the geometric center. Moreover, the rate of slowdown quantitatively agrees with the experimental results (Figure 4I, colored points). The recapitulation of the nontrivial dynamic transformation of the uniaxial steady-state condition into the symmetric double-headed state provides strong support for our model and its underlying assumptions.

Ft/Ds Mediates the M/L Polarization Component

With distinct \vec{A} and \vec{M} fields as key elements of our model, the orientation of ciliary rootlets along the A/P and M/L axes should

consequently involve functionally separable molecular activities. Toward the goal of identifying corresponding molecules, we first simulated the loss of the M/L polarization component (either by inactivation of the boundary cue, $\alpha_B = 0$, or loss of the cellular response to it, $\delta_M = 0$, see Figure 4B). With uniform A/P orientation and loss of splay as predicted loss of function phenotype (Figure 5A), we turned to RNAi screening. An inspection of Smed transcriptome and genome resources in PlanMine (Rozanski et al., 2019) revealed homologs of multiple polarity pathways, including the Ft/Ds pathway. Specifically, Smed harbors a single homolog of Dachsous (*Smed-ds*), at least 2 homologs of Fat (*Smed-ft-1* and *Smed-ft-2*), 2 homologs of Dachs (*Smed-dachs-1* and *Smed-dachs-2*), and a single homolog of Four-jointed (*Smed-fj*). Except for *fj*, all genes are broadly expressed in the epidermis and various other cell types (Figures 5B and S5A–S5C), with *ds* additionally displaying prominent expression in epidermal cells along the body margin. Intriguingly, RNAi against the single *ds* homolog in non-regenerating animals (referred to as “intact” below) strikingly recapitulated the M/L component-loss prediction (Figure 5C); *ds*(RNAi) animals invariably displayed strongly reduced splay all along the A/P axis (Figure 5D) and consequent statistically significant reductions in the slope of M/L polarity trajectories in head, trunk, and tail (Figure 5E). The decay of the spatial autocorrelation function and average rootlet polarization along the A/P axis were unaffected (Figures S5E and S5F), indicating that Ds is required neither for A/P rootlet orientation nor for rotational rootlet polarity within individual cells. Together with the very similar phenotypes of *ft-1*, *ft-2*(RNAi) animals (Figures S5G and S5H), these data indicate a specific role of the Smed Ft/Ds pathway in orienting ciliary rootlets toward the body margins.

To examine the extent by which Ft/Ds pathway function conforms to the M/L polarity component of our model, we used the anterior polarity reversal in “headless” *pbx*(RNAi) animals as a test case. Since our model rationalizes this phenotype as unopposed dominance of the radially acting M/L component, inactivation of the M/L component should consequently rescue the anterior polarity reversal (Figure 5F). Indeed, the additional inactivation of *ds* in *pbx*(RNAi) trunk pieces resulted in a much-reduced anterior polarity reversal (Figures 5G and 5H), despite similar knockdown efficiencies as in single RNAi experiments (Figure S5I). Moreover, the double knockdown restored the splay gradient along the A/P axis that *ds*(RNAi) alone abolishes (Figures 5G and S5K). Our model could replicate this effect by simply combining the parameter settings of the single knockdown simulations (reduced A/P component in *pbx*(RNAi)) and

(B) Vector field representation of average rootlet orientation within 100 μ m bins of a representative specimen. Scale bar: 250 μ m.

(C) A/P-polarization component in double-headed specimens.

(D) Double-tailed Smed regenerated from an APC(RNAi) trunk piece. Left: Live image. Right: Head, trunk, and tail marker expression by *in situ* hybridization. Scale bar: 500 μ m.

(E) Vector field representation of average rootlet orientation within 100 μ m bins of a representative double-tailed specimen. Scale bar: 250 μ m.

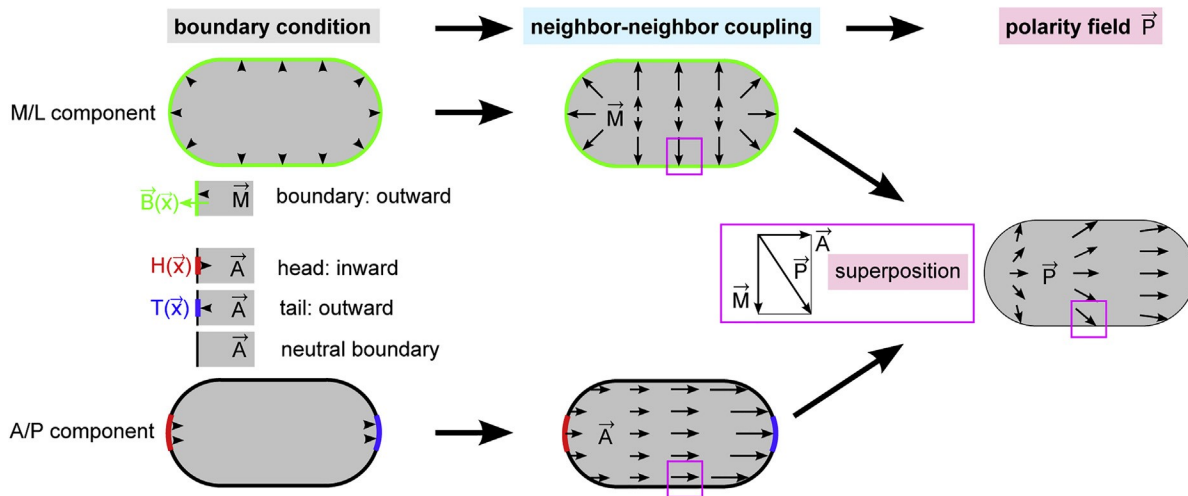
(F) A/P-polarization component in double-tailed specimens.

(G) Headless and tailless Smed regenerated from a *pbx*(RNAi) trunk piece. Left: Live image. Right: Head, trunk, and tail marker expression by *in situ* hybridization. Scale bar: 500 μ m.

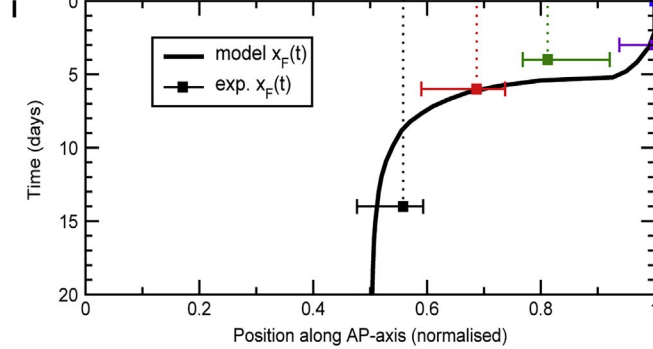
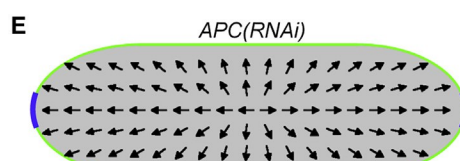
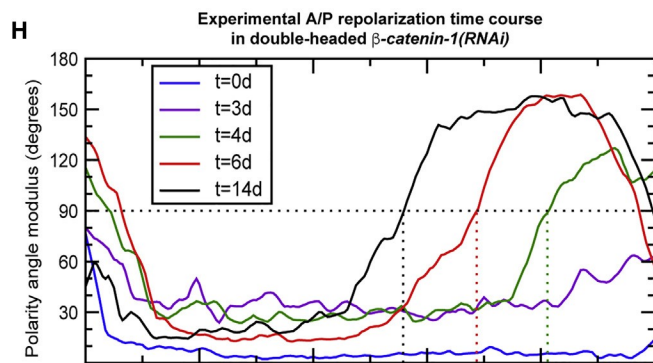
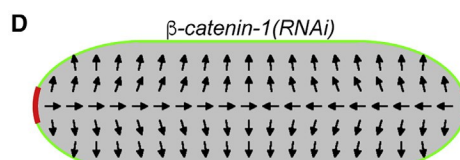
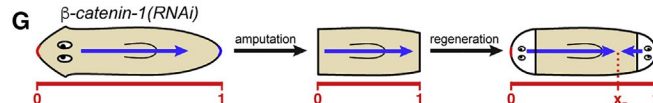
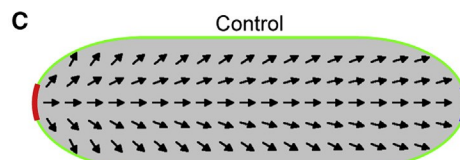
(H) Vector field representation of average rootlet orientation within 100 μ m bins of a representative headless and tailless specimen. Scale bar: 250 μ m.

(I) A/P-polarization component in headless and tailless specimens.

(C, F, and I) $n = 6$ specimens each at 14 days of regeneration, colored lines: individual length-normalized specimens. Rootlet orientation was averaged orthogonal to the midline. Mean and SD: solid black line and grey shading. Dashed line: average of six wild-type specimens. 0° designates head to tail, $+/- 90^\circ$ orthogonal orientations and cartoons illustrate measured results.

A Model assumptions**B Model equations**

$$\begin{aligned} \dot{\vec{A}} &= (\alpha_T \textcolor{blue}{T} - \alpha_H \textcolor{red}{H}) \vec{B} - (\beta_T \textcolor{blue}{T} + \beta_H \textcolor{red}{H}) \vec{A} & - \gamma_A \vec{A} &+ D_A \nabla^2 \vec{A} \\ \dot{\vec{M}} &= \alpha_B \vec{B} & - \gamma_M \vec{M} &+ D_M \nabla^2 \vec{M} \end{aligned} \quad \rightarrow \quad \vec{P} = \frac{\delta_A \vec{A} + \delta_M \vec{M}}{\|\delta_A \vec{A} + \delta_M \vec{M}\|}$$



F pbx (RNAi) (t=short)

Figure 4. Polarity Field Modeling

(A) Implementation of boundary effects (left, gray boxes), neighbor-neighbor coupling (center, blue boxes), and linear superposition (pink, right section) of the radially directed M/L field $\vec{M}(\vec{x})$ and the axially directed A/P field $\vec{A}(\vec{x})$. The resulting unit vector field \vec{P} represents actual ciliary rootlet orientation.

reduced M/L component in *ds(RNAi)*; Figure S4E) without any parameter tuning, which thus validates the emergence of rootlet orientation (\vec{P}) out of the superposition of distinct A/P and M/L components (Figure 4A). Overall, the ability of *ds(RNAi)* to rescue the *pbx(RNAi)* phenotype conclusively establishes the body margin as a polarity organizer and the planarian Ft/Ds pathway as molecular mediator of our model's M/L component.

Core PCP Signaling Mediates A/P Polarization

To further identify molecular mediators of our model's A/P component, we simulated the expected loss of the A/P component and identified the radial reorientation of rootlets due to unopposed dominance of the M/L polarization component as predicted loss of function phenotype of A/P polarity components (Figure 6A). Smed harbors multiple homologs of the core PCP pathway (e.g., a total of nine *fz* homologs (Liu et al., 2013; Stückemann et al., 2017), three *vang* homologs (Almuedo-Castillo et al., 2011), and two *dvl* homologs (Gurley et al., 2008), but no clear homologues of *fmi/celsr* or *pk* so far), which are expressed in epithelial cells, but also other cell types (Figures S6A–S6C). To analyze putative contributions of the core PCP pathway to rootlet polarization, we first targeted the two Smed *dvl* homologs in intact animals. Rootlet morphology and numbers appeared normal in *Smed-dvl-1,-2(RNAi)* specimens (Figures 6B and S6D), even though the observed tail loss (Figure 6C) due to concomitant canonical Wnt inhibition (Gurley et al., 2008) indicated efficient gene knockdown. This finding was unexpected due to the requirement of *Xenopus dvl* for basal body docking (Park et al., 2008) and the previous inference of similar roles in planarians (Almuedo-Castillo et al., 2011). Intriguingly, the measured epidermal polarity field in the *Smed-dvl-1,-2(RNAi)* animals displayed a strong and global reorientation towards the body edge (Figures 6E and 6F), corresponding to the predicted A/P-component loss of function phenotype (Figure 6D). Although the more rapid decay of the spatial autocorrelation function indicated weakened neighbor–neighbor coupling (Figure S6E), *dvl-1,-2(RNAi)* animals clearly maintained rotational and planar rootlet polarization within and between epidermal cells. Also, the simultaneous knockdown of the two homologs of the core PCP-specific component Vang resulted in a marked and statistically significant splay increase, particularly in central and posterior body regions (Figures 6G, 6H, and S6E), yet without discernible effects on tail maintenance (Figure S6G). By extension, the *Smed-dvl-1,-2(RNAi)* phenotype is therefore unlikely due to tail-determinant loss (Figure 6C) and our results generally implicate the planarian core PCP pathway in the orientation of ciliary rootlets along the A/P axis.

To examine the extent to which core PCP function conforms to the A/P polarity component of our model, we next examined the

interplay between A/P and M/L components. Our model predicts the rescue of the A/P component-loss-induced radial polarization by the additional inactivation of the M/L component (since decreasing both \vec{A} and \vec{M} by the same factor has no effect on their normalized sum \vec{P} , see Figures 4B and 6I). We experimentally realized this scenario by additionally targeting *ds* in *dvl-1,-2(RNAi)* animals; qPCR experiments confirmed similar knockdown efficiencies in the triple knockdowns as compared to double or single RNAi treatments (Figure S7A). Strikingly, *ds/dvl-1,-2(RNAi)* animals nevertheless displayed near wild-type epidermal polarity fields (Figures 6J, 6K, S7B, and S7C), which we could recapitulate by simply combining the parameter settings of the individual *ds(RNAi)* and *dvl-1,-2(RNAi)* simulations in our model (Figure S4H). The rescue of the *dvl-1,-2(RNAi)* phenotype by *ds(RNAi)* thus strongly suggests that the planarian core-PCP pathway is indeed the molecular mediator of our model's A/P component. Moreover, these results also demonstrate that the wild-type polarity field does not depend on the absolute strength of polarity cues, but on their ratio. Together with the restoration of the splay in *ds/pbx(RNAi)*, these findings, therefore, also provide experimental support for the emergence of rootlet orientation (\vec{P}) out of the superposition of distinct A/P and M/L components (Figure 4A) and thus for another central premise of our model. Overall, our results establish a framework for the alignment of ciliary rootlets relative to the global landmarks of the planarian body plan.

DISCUSSION

Model

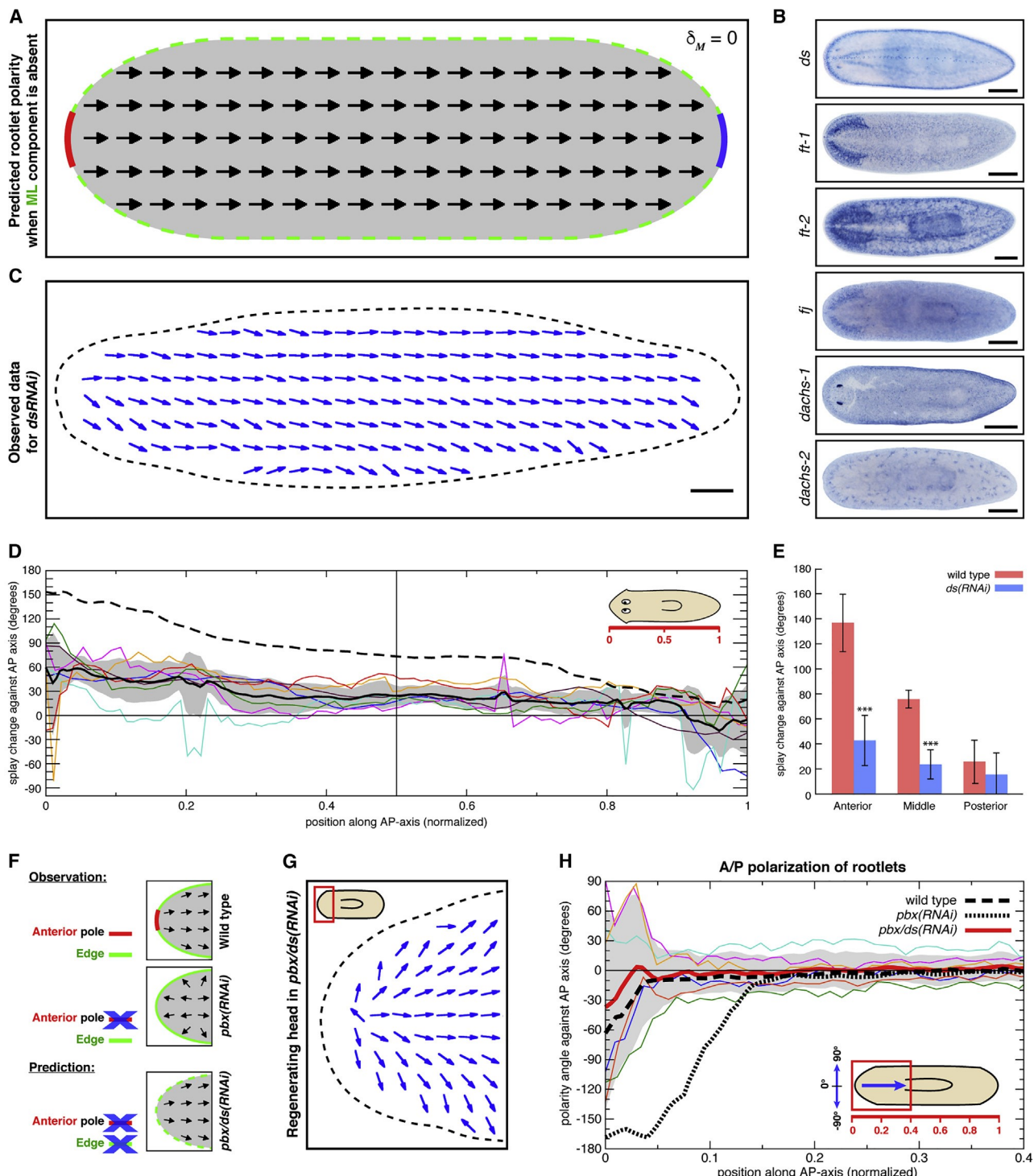
Here, we investigate the planar polarization of the MCCs within the Smed ventral epidermis by example of ciliary rootlet orientation. Our results demonstrate that the local planar polarization of rootlet orientation is a dynamic phenomenon that rapidly responds to global body plan polarity alterations. With the extensive mechanistic understanding of core PCP- and Ft/Ds-mediated polarization pathways as foundational basis (Adler, 2012; Aw and Devenport, 2017; Butler and Wallingford, 2017; Goodrich and Strutt, 2011; Wallingford, 2010; Yang and Mlodzik, 2015), our results suggest the following model for the polarization of the planarian epidermis (Figure 7). At the cellular level (top panel), the differential subcellular localization of the core PCP (red and blue) and Ft/Ds (green) pathway components establishes independent polarity vectors within epidermal cells. The rotational polarity vector of ciliary rootlets (gray) orients along the sum (gray arrow) of the two vectors. At the organismal level (bottom panel), the anterior and posterior termini of the midline (head and tail poles; red and blue) and the body margin (green) set the core PCP and Ft/Ds vectors of adjacent epidermal

(B) Model equations for the temporal dynamics of $\vec{A}(\vec{x}, t)$ and $\vec{M}(\vec{x}, t)$ and the algebraic result $\vec{P}(\vec{x}, t)$. Details in STAR Methods.

(C–F) Simulations of wild-type (C), double-headed (D), double-tailed (E) and headless-tailless (F) polarity fields. All simulations were initialized with wild-type parameters and only the boundary conditions for the head and tail ($H(\vec{x})$, $T(\vec{x})$) were changed as cartooned. (C–E) final states; (F) a temporal intermediate.

(G) Experimental design probing A/P polarity reversal dynamics upon ectopic head induction.

(H and I) Rootlet repolarization time course in regenerating β -catenin-1(RNAi) trunk pieces. (H) Averaged A/P orientation at indicated time points ($n = 6$ /time point; see Figure S4M). The 4-day trace (green) signifies the onset of the polarity reversal (right), which propagates to the center by day 14 (black trace). The spike at the opposite anterior end is an artifact of our surface extraction procedure. Dashed lines: Position of the repolarization front, defined by a polarity value of 90° (i.e., the point of polarity inversion from wild type [0°] to ectopic [180°] orientation; see Figure S4M for original data). (I) Measured (mean \pm SD) versus predicted (solid curve) position of the repolarization front at indicated time points. The predicted $x_F(t)$ trace was simulated on the basis of the steady-state wild-type parameter set (C) and 1 h as universal time unit of all model parameters. See STAR Methods for details.

**Figure 5. Ft/Ds Mediates the M/L Polarity Component**(A) Predicted rootlet orientation in absence of the M/L component ($\delta_M = 0$).(B) Expression patterns of Smed Ft/Ds pathway genes by whole mount *in situ* hybridization. Scale bar: 500 μ m.(C) Vector field representation of average rootlet orientation within 100 μ m bins of a representative intact *ds(RNAi)* specimen. Scale bar: 250 μ m.(D) Splay angle change along the A/P axis of intact planarians under *ds(RNAi)*; $n = 7$ specimens (colored lines), traces were length normalized. Average and standard deviation: solid black line and gray shading. Dashed line: average of six wild-type specimens. 0° : uniform A/P orientation; 180° : orientation toward the margins.

(legend continued on next page)

cells. Cell-cell coupling (middle panel) via the established transinteractions of the transmembrane components of the two polarity pathways propagates the boundary effects across the tissue and ultimately to the ciliary rootlets of individual cells. The epidermal polarity field thus emerges as a consequence of spatially restricted boundary effects and their differential superposition (middle panel). Our model rationalizes the polarity reversal of ciliary rootlets in response to ectopic head or tail induction (Figures 3A–3F, 4D, and 4E) and also the repolarization dynamics (Figures 4G–4I). Further, the interplay between the independent A/P and M/L components explains the head-tail gradation of the splay in wild-type animals (Figures 2F–2H), the anterior-specific polarity reversal in “headless and tailless” *pbx(RNAi)* animals (Figures 3H and 3I), its rescue upon concomitant knockdown of Ft/Ds components (Figures 5G and 5H), and the seemingly paradoxical restoration of A/P orientation under simultaneous inhibition of Ft/Ds and core PCP (Figures 6J, JK, S4C, S4G, and S4H). Overall, our model thus provides a mechanistic framework that rationalizes the orientation of ciliary rootlets at the subcellular level relative to global body plan landmarks.

Our demonstration of functionally segregable A/P and M/L polarization components, and of core PCP and Ft/Ds as their specific molecular mediators, provides a strong rationale for the two-field assumption in our mathematical model (Figure 4), even though the superposition of two fields may seem nonparsimonious. Indeed, a single polarity field (e.g., direct coupling of H, T, and B to \vec{P}) is broadly sufficient for the transmission of the boundary effects (data not shown). The strongly margin-enriched expression of *ds* (Figure 5B) and more uniform core PCP expression (Figure S6A) could further represent the biological manifestation of such a one-field scenario, specifically as *ds*-mediated boundary condition modulation of a panepidermal core PCP polarity field. While the transcriptional upregulation of *ds* under both *dvl-1,-2(RNAi)* and *vangl-1,-2(RNAi)* (Figures S6F and S7A) and the concomitant radial reorientation of the epidermal polarity field provides some evidence for such a mechanism, our results currently cannot ascertain whether the *ds* upregulation occurs in the epidermis or in one of the other *ds* and core PCP expressing tissues (Figures S5A–S5C and S6A–S6C). A further possibility that our current data cannot exclude is that Ft/Ds and core PCP influence epidermal polarization indirectly, for example, via the polarization of muscle fiber orientation in the body wall musculature immediately beneath the epidermis (Scimone et al., 2017). The direct visualization of subcellular Ft/Ds and core PCP complex distribution will be essential for distinguishing between independent or parallel functions of core PCP and Ft/Ds, or between cell-autonomous versus nonautonomous effects on epidermal polarization. Nevertheless, our results clearly establish that the ciliary rootlets in the planarian epidermis orient according to polarity inputs

from both core PCP and Ft/Ds. To our knowledge, this is the first demonstration of functionally segregable and simultaneous contributions of both pathways to planar cell polarization outside of the *Drosophila* wing disk, which therefore establishes the interplay between core PCP and Ft/Ds as an evolutionarily conserved 2D-polarization module.

Origins of Polarity

Our results demonstrate the repolarization of the epidermis by ectopically induced heads, which is interesting also because of the *de novo* induction of a tissue polarity vector within a fully polarized adult tissue. Analogous experiments are difficult in embryonic PCP systems, as polarity vectors often emerge concomitantly with planar cell polarization *per se*. Our data implicate the so-called pole cells as the source of the epidermal A/P polarization cue. The pole cells are a group of specialized muscle cells at the head and tail tip that are thought to function analogously to embryonic organizers in specifying axial-tissue identity (Blassberg et al., 2013; Chen et al., 2013; Reuter et al., 2015; Li et al., 2019; Oderberg et al., 2017; Reddien, 2018; Rink, 2018; Scimone et al., 2014; Vásquez-Doorman and Petersen, 2014; Vogg et al., 2014). Their *pbx*-dependent differentiation and convergence at the future head or tail tip by ~ 3 days of regeneration (Oderberg et al., 2017) coincide with the timing of repolarization front initiation (Figures 4H–4I). Further, the head-tip-centered geometry of the splay pattern in wild-type animals (Figure 2) and the *pbx* dependence at least of the head polarity cue (Figures 3G–3I) are all consistent with the pole cells as localized A/P polarity determinants and thus as cell biological mediators of the boundary condition in our model. The implied dual roles of the poles as organizers of tissue identity and tissue polarity further resemble similarly dual roles of many developmental organizers (Chu and Sokol, 2016; Dahmann et al., 2011; Sagner et al., 2012) and likely reflects a conserved strategy that ensures the alignment of tissue polarity vectors with the cardinal body axes.

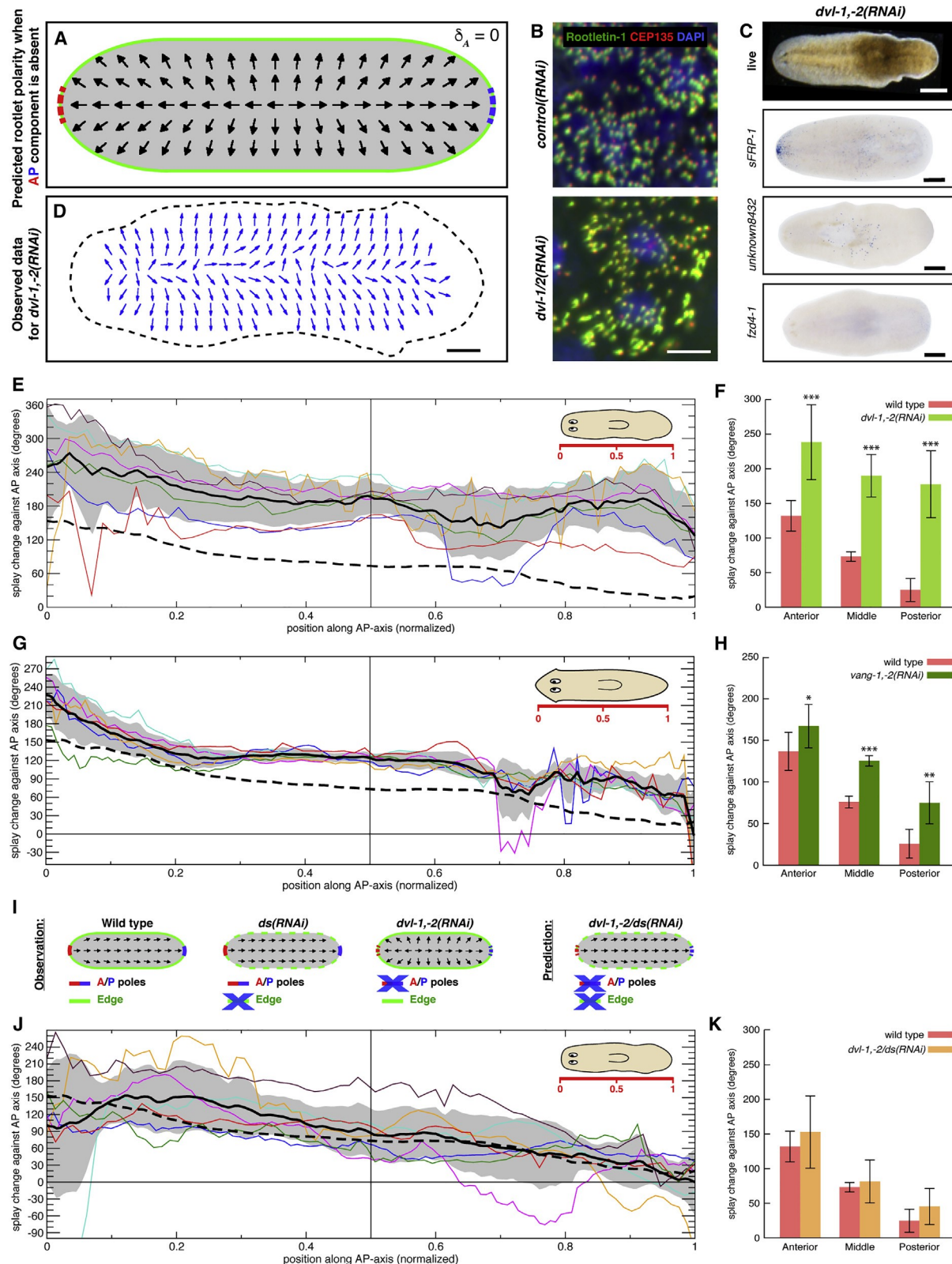
At present, we can only speculate on how the poles might specify polarity vectors. The global loss of A/P polarization that we observe upon interference with *dvl* and *vangl-1,-2* (Figures 6D–6H) indicates that both poles exert their A/P-polarizing effect via the core PCP pathway, despite the independent and opposite polarizing effects of head and tail (Figures 3A–3F). The “domineering nonautonomy” of core-PCP mutant clones in the *Drosophila* wing disk provide an interesting conceptual analogy for the specification of opposite polarity vectors by a single pathway. Clone boundaries of *fz* or *vang* orient wing hairs in opposite directions in the surrounding wild-type tissue (Taylor et al., 1998; Vinson and Adler, 1987), which is thought to result out of the interplay between intracellular Fz and Vang complex antagonism and intercellular coupling of Fz/Vang complexes via the mutual affinity of their extracellular domains

(E) Quantitative splay angle comparison between *ds(RNAi)* ($n = 7$) and wild-type ($n = 6$) specimens. Bars display splay angle averages in head, trunk, and tail. Error bars: \pm SD. * $p < 0.05$; ** $p < 0.01$; *** $p < 0.001$.

(F) Rationale of the double-RNAi experiment.

(G) Vector field representation of average rootlet orientation within 100 μm bins of a representative headless *pbx/ds(RNAi)* specimen.

(H) Averaged rootlet orientation orthogonal to the midline within the indicated region of *pbx/ds(RNAi)* specimens, $n = 6$ (colored lines). Gray shading: SD of the local mean. Traces are length normalized. Bold lines: mean of *pbx/ds(RNAi)*, wild-type and *pbx(RNAi)* as indicated. 0°: head to tail orientation; $\pm 180^\circ$: the opposite directionality.

**Figure 6. Core PCP Mediates the A/P Polarity Component**(A) Predicted rootlet orientation in absence of the A/P polarity component ($\delta_A = 0$).(B) Anti-ROOTLETIN-1 (green) and anti-CEP135 (red) antibody staining in control (top) and *dvl-1,-2(RNAi)* (bottom); nuclei are in blue (Hoechst). Scale bar: 5 μ m.

(legend continued on next page)

(Amonlirdviman et al., 2005). Analogously, the “repulsive” versus “attractive” influence of the planarian head or tail on epidermal polarity could reflect “domineering nonautonomy” on the organismal scale, specifically the pole-dependent stabilization of either one of the two core PCP complexes at the head or tail tip (Figure 7). While the many Wnt ligands that are expressed in the planarian tail in a tail-pole-dependent manner (Chen et al., 2013; Gurley et al., 2010; Petersen and Reddien, 2009) and the destabilizing effect of Wnt ligands on surface-localized Fz complexes in *Drosophila* (Wu et al., 2013) provide a plausible scenario for tail-polarity vector specification, analogous activities that target Vang and thus might mediate the specification of the planarian head vector have so far not been demonstrated in any system. Smed offers experimental opportunities to identify such activities, for example, via double-RNAi screens for phenotypes that uncouple β -catenin-1(RNAi) mediated ectopic head induction from epidermal repolarization. More generally, the clearcut cause-and-effect relationship between ectopic head (and likely also tail) induction and epidermal repolarization provides a compelling experimental paradigm for addressing the mechanistic origins of tissue polarity, which have proven difficult to understand in developmental polarity systems.

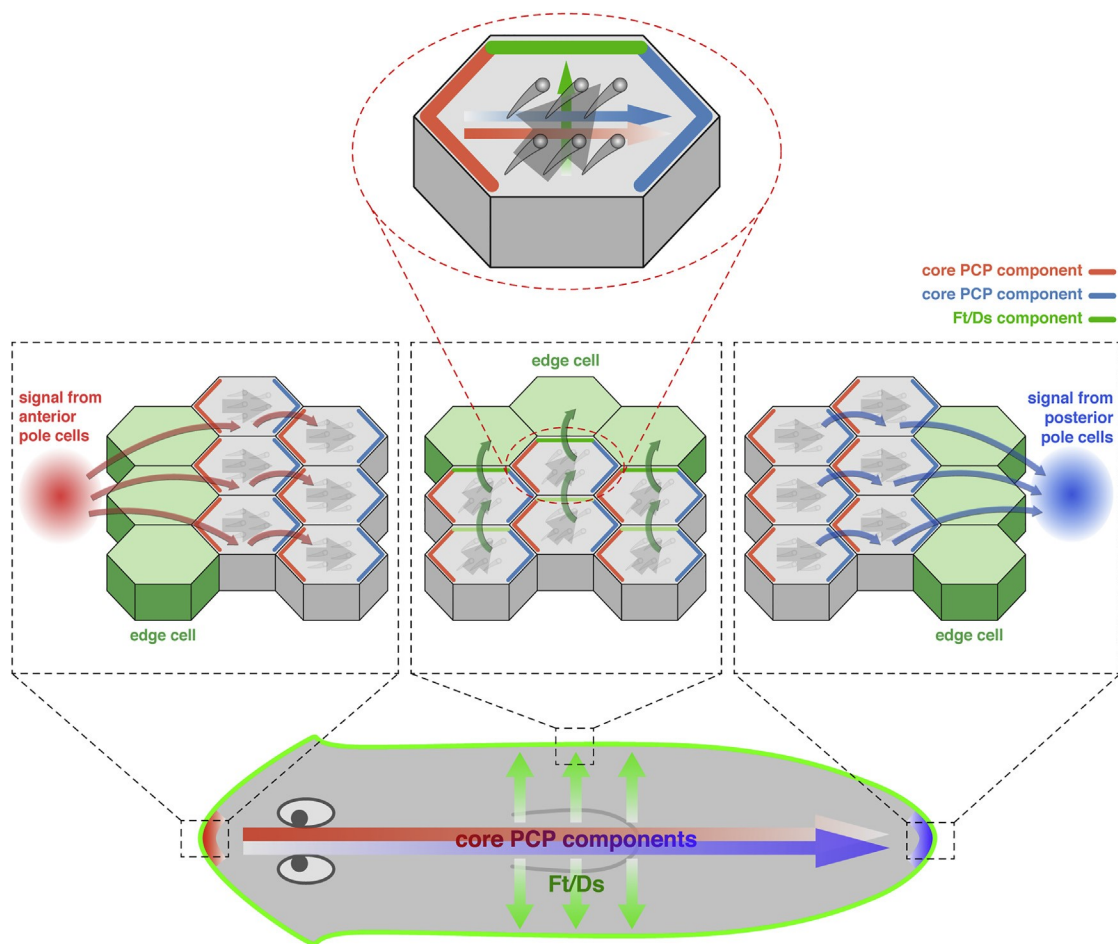
Polarity Dynamics

A further fascinating feature of the planar polarization of the planarian epidermis is its highly dynamic nature. The conversion of a uniaxially polarized trunk piece into a symmetric bipolar double-headed state over the course of approximately ten days (Figures 4H–4I) provides a striking case in point. Our time course experiments clearly show that the polarity reversal initiates at the boundary in the vicinity of the future ectopic head tip, from where it spreads into the adjacent tissue in a seemingly highly coordinated manner. Although our current pipeline’s coarse graining of rootlet orientation in 150-pixel squares precludes the quantification of cellular and subcellular phenomena, the steep transition between oppositely polarized regions at all time points (Figure S4M) indicates that the polarity reversal entails an only transient loss of polarity, if at all. Hence, the polarity reversal likely occurs by a rapid and locally coordinated inversion of rootlet orientation, which propagates in a wave-like manner from the site of the symmetry-breaking event at the boundary. Not only are the observed dynamics qualitatively consistent with the central assumptions of our model (Figure 7), but the model also provides a nontrivial rationale for the observed gradual slow down of the repolarization front (Figure 4I). This effect arises from our implementation of polarity propagation via a nondirectional diffusion term that we previously showed to emerge from

the discrete coupling of each cell’s polarity vector toward the average of its neighbors (Hoffmann et al., 2017; Merkel et al., 2014). Consequently, the influence of the boundary state weakens as a function of distance from the ectopic head tip and the repolarization front halts once the local influence of both heads is equal, i.e., at the geometric midpoint of double-headed animals (Figure 3B).

One of the interesting questions raised by these findings is the cell biological mechanism of front progression. Data from a variety of systems indicates that ciliary rootlets assemble in a grid-like manner within individual MCC (Lemul-lois et al., 1988; Reed et al., 1984; Werner et al., 2011) and that the rotational orientation of the grid is in turn determined by cytoskeletal links to junctional core PCP complexes (Mitchell et al., 2009; Vladar et al., 2012). Accordingly, the progression of the repolarization front can be envisaged as locally coordinated rotation of rootlet grids, possibly as a consequence of dynamically reorienting junctional PCP complexes. However, the MCCs of the planarian epidermis are themselves highly dynamic and undergo continuous replacement by the integration of postmitotic progenitors from deeper tissue layers (Reddien et al., 2005; Tu et al., 2015; van Wolfswinkel et al., 2014). Thus, front progression could also be envisaged by means of MCC progenitor integration with reversed polarity. Although we are currently lacking the tools to explicitly distinguish between the two scenarios, we failed to observe indications of the systematic reduction in cell size and rootlet number/cell at the propagation front that would be expected from an immature progenitor integration wave. A further interesting observation is that the polarity reversal in headless and tailless *pbx*(RNAi) animals remains restricted to newly formed tissues 14 days post-amputation (Figure 3H), while reaching the geometric center of the pre-existing tissue in the case of ectopic head-induced repolarization (Figure 3B). Possible explanations include weaker Ft/Ds versus core PCP-mediated neighbor–neighbor coupling and a consequently faster decay of the boundary influence (see above) or the differential susceptibility of new versus old tissue to repolarization, which is not part of the current model. More generally, the experimental reversibility of an adult epidermal polarity field that we demonstrate promises an interesting test case for current challenges in planar cell polarization, for example, the contribution of junctional PCP complex dynamics to vector specification (Warrington et al., 2017) or the cause or consequence interplay between PCP complex and cytoskeletal polarization during rootlet reorientation (Herawati et al., 2016; Vladar et al., 2012).

- (C) Live-image (top) and head, trunk, and tail marker expression by *in situ* hybridization (below) in intact *dvl-1,-2(RNAi)* specimens. Scale bar: 500 μ m.
 (D) Vector field representation of the average ciliary rootlet orientation within 100 μ m squares of a representative intact *dvl-1,-2(RNAi)* specimen. Scale bar: 250 μ m.
 (E) Splay angle change along the A/P axis of intact *dvl-1,-2(RNAi)* specimens ($n = 6$).
 (F) Quantitative splay angle comparison between intact *dvl-1,-2(RNAi)*, and wild-type, based on (E).
 (G) Splay angle change along the A/P axis of intact *vang-1,-2(RNAi)* specimens ($n = 6$).
 (H) Quantitative splay angle comparison between *vang-1,-2(RNAi)*, and wild type, based on (G).
 (I) Rationale of *dvl-1,-2/ds* triple-RNAi experiment. See text for details.
 (J) Splay angle change along the A/P axis of intact *dvl-1,-2/ds(RNAi)* specimens ($n = 6$).
 (K) Quantitative splay angle comparison between *dvl-1,-2/ds(RNAi)*, and wild-type, based on (J).
 (F, H, and K) Bars: splay angle averages within head, trunk, and tail territories. Error bars: $+/-\text{SD}$; \times p value < 0.05 ; $**$ p value < 0.01 ; $***$ p value < 0.001 .
 (E, G, and J) Shading: SD of the mean (solid black). Dashed line: average of six wild-type specimens. 0° designates uniform A/P orientation, 180° M/L orientation.

**Figure 7. Model**

Multi-scale polarity coordination in planarians. See text for details.

Long-Range Coordination of Polarity

A final challenge that the planarian epidermis epitomizes is the generation and maintenance of coherent polarity fields across hundreds or even thousands of cell diameters. The conceptual interest in this problem stems from the frequent observation of so-called swirls, localized circular deviations of the tissue scale polarity field, in PCP mutant tissues (Antic et al., 2010; Mitchell et al., 2009; Taylor et al., 1998; Vinson and Adler, 1987; Wong and Adler, 1993). Moreover, simulations of the dynamic intra- and intercellular PCP feedback interactions suggest an inherent tendency of self-organized polarity systems to get trapped in swirl-like local energy minima (Amonlirdviman et al., 2005; Burak and Shraiman, 2009; Hazelwood and Hancock, 2013). At up to 25 mm of body length, *Smed* exceeds the length scale of the *Drosophila* wing disk by > 2 orders of magnitude and should thus be highly susceptible to swirl formation. Hence, it is surprising that we failed to observe swirls under our experimental conditions. Moreover, the Ft/Ds or core PCP(RNAi)-induced epidermal polarity field alterations that we observe (Figures 5C–5E and 6D–6H) still maintain long-range polarity coordination, which is even more strikingly emphasized by the “rescue” of A/P polarization by simultaneous inactivation of both path-

ways (Figures 6J and 6K). Although we cannot exclude that incomplete gene knockdown (Figures S5I and S6F) or the coarse graining of cilia orientation within 150-pixel squares preclude swirl detection under our experimental conditions, it is important to also point out that simultaneous genetic inactivation of both PCP pathways in the *Drosophila* wing also do not abolish tissue-scale polarity (Sagner et al., 2012). Moreover, individual *Drosophila* PCP mutants result in characteristic and highly reproducible wing hair swirl patterns (Taylor et al., 1998; Vinson and Adler, 1987; Wong and Adler, 1993). Rather than reflecting the random breakdown of long-range polarity coordination, swirls therefore can be seen as the aberrant reorientations of a persisting tissue-scale polarity field. Overall, this leads to the conclusion that the evolutionarily conserved function of the PCP pathways is the alignment of tissue polarity fields to specific landmarks, but that they are neither necessary for cell polarity per se, nor for the planar coordination of polarity vectors between neighboring cells.

If not the planar cell polarity pathways, what then accounts for intrinsic cell polarity and its coordination at the tissue scale? To our knowledge, not a single *Drosophila* mutant is known that truly randomizes wing hair orientation, and the randomization of

ciliary rootlet orientation in MCCs appears to invariably involve defective basal body docking to the cell cortex (Adler, 2002; Adler and Wallingford, 2017; Meunier and Azimzadeh, 2016; Park et al., 2008). Although it is conceivable that key mechanisms have escaped discovery thus far, an alternative possibility is that polarized wing hair outgrowth or polarized rootlet self-assembly within the cell cortex signify cell polarity *per se*, rather than a secondary consequence of a cryptic polarity signal. Further, the flow-induced refinement of motile cilia alignment in MCCs (Guirao et al., 2010; Mitchell et al., 2007) or mechanical feedback between wing-hair outgrowth-induced stresses and the established orienting influence of stress on tissue polarity (Aigouy et al., 2010; Chien et al., 2015) provide conceivable mechanisms for local polarity coordination. Such a material-property-centric view of PCP further establishes conceptual parallels to the striking long-range polarity patterns that can emerge in abiotic liquid crystal textures (Chaikin and Lubensky, 2000), and the recently proposed dynamic alignment of mouse-airway epithelial cell rootlets by cortical actin flows is strongly reminiscent of a liquid crystal system (Herawati et al., 2016). Nevertheless, the challenge remains to identify an explicit material basis of planar cell polarity, corresponding orienting principles at the tissue scale, and the nature of the conserved interactions between the core PCP pathways and the resulting polarity fields. With their phylogenetic distance to established PCP model systems and the dynamic repolarization of a polarized adult epidermis as chief experimental asset, planarians can be expected to contribute meaningful insights.

STAR★METHODS

Detailed methods are provided in the online version of this paper and include the following:

- **KEY RESOURCES TABLE**
- **LEAD CONTACT AND MATERIALS AVAILABILITY**
- **EXPERIMENTAL MODEL AND SUBJECT DETAILS**
 - Schmidtea mediterranea
- **METHOD DETAILS**
 - Cloning and RNA-Mediated Gene Silencing
 - Recombinant Protein and Antibody Production
 - Electron Microscopy
 - Whole-Mount Antibody Staining
 - *In Situ* Hybridization
 - qPCR
 - Light Microscopy and Image Analysis
 - Details on the Model Equations
 - Simulation Details
 - Parameter Estimation
- **QUANTIFICATION AND STATISTICAL ANALYSIS**
 - Rootlet Detection and Orientation Quantification
 - Mathematical Methods for Ciliary Rootlet Statistics
- **DATA AND CODE AVAILABILITY**

SUPPLEMENTAL INFORMATION

Supplemental Information can be found online at <https://doi.org/10.1016/j.decel.2019.10.022>.

ACKNOWLEDGMENTS

We thank Drs. Carl Modes, Frank Jülicher, and the late Suzanne Eaton for comments on the manuscript. We gratefully acknowledge Suzanne Eaton's insights, ideas, and enthusiasm that shaped both this manuscript and the PCP community. We thank Julian Rode, Jörn Starruß, Stephanie von Kannen, and Heino Andreas for technical support and Rink lab members for lively discussions. We thank the following MPI-CBG facilities for their support: Antibody Facility, Protein Expression Facility, Light Microscopy Facility, Electron Microscopy Facility, and Media Kitchen. The simulations and statistical analysis were performed on High Performance Computing resources provided by the ZIH at TU Dresden. This work was supported by the grant 0316169A+B "Virtual Planarian" as part of the German Federal Ministry of Education and Research (BMBF) e:Bio initiative (L.B. and J.C.R.), grant 031L0159B within the BMBF e:Med initiative (L.B.), grant 391070520 by Deutsche Forschungsgemeinschaft DFG (L.B.), and by Max Planck Society funding (J.C.R.).

AUTHOR CONTRIBUTIONS

Conceptualization, L.B. and J.C.R.; Methodology, C.B., M.K., S.M., and H.T.-K.V.; Investigation, J.A., C.B., M.K., S.M., and H.T.-K.V.; Visualization, L.B., M.K., S.M., J.C.R., and H.T.-K.V.; Writing – Original Draft, L.B. and J.C.R.; Writing – Review and Editing, L.B., M.K., J.C.R., and H.T.-K.V.; Funding Acquisition, L.B. and J.C.R.; Supervision, J.C.R., L.B., and E.W.G.

DECLARATION OF INTERESTS

The authors declare no competing interests.

Received: April 30, 2018

Revised: July 15, 2019

Accepted: October 23, 2019

Published: November 18, 2019

REFERENCES

- Adler, P.N. (2002). Planar signaling and morphogenesis in *Drosophila*. *Dev. Cell* 2, 525–535.
- Adler, P.N. (2012). The frizzled/stan pathway and planar cell polarity in the *Drosophila* wing. *Curr. Top. Dev. Biol.* 101, 1–31.
- Adler, P.N., and Wallingford, J.B. (2017). From planar cell polarity to ciliogenesis and back: the curious tale of the PPE and Cplane proteins. *Trends Cell Biol.* 27, 379–390.
- Aigouy, B., Farhadifar, R., Staple, D.B., Sagner, A., Röper, J.C., Jülicher, F., and Eaton, S. (2010). Cell flow reorients the axis of planar polarity in the wing epithelium of *Drosophila*. *Cell* 142, 773–786.
- Almuedo-Castillo, M., Saló, E., and Adell, T. (2011). Dishevelled is essential for neural connectivity and planar cell polarity in planarians. *Proc. Natl. Acad. Sci. U.S.A.* 108, 2813–2818.
- Alvarado, A.S. (2002). The *Schmidtea mediterranea* database as a molecular resource for studying platyhelminthes, stem cells and regeneration. *Development* 129, 5659–5665.
- Amonlirdviman, K., Khare, N.A., Tree, D.R.P., Chen, W.S., Axelrod, J.D., and Tomlin, C.J. (2005). Mathematical modeling of planar cell polarity to understand domineering nonautonomy. *Science* 307, 423–426.
- Antic, D., Stubbs, J.L., Suyama, K., Kintner, C., Scott, M.P., and Axelrod, J.D. (2010). Planar cell polarity enables posterior localization of nodal cilia and left-right axis determination during mouse and *Xenopus* embryogenesis. *PLoS One* 5, e8999.
- Aslanidis, C., and de Jong, P.J. (1990). Ligation-independent cloning of PCR products (LIC-PCR). *Nucleic Acids Res.* 18, 6069–6074.
- Aw, W.Y., and Devenport, D. (2017). Planar cell polarity: global inputs establishing cellular asymmetry. *Curr. Opin. Cell Biol.* 44, 110–116.
- Azimzadeh, J., Wong, M.L., Downhour, D.M., Sánchez Alvarado, A.S., and Marshall, W.F. (2012). Centrosome loss in the evolution of planarians. *Science* 335, 461–463.

- Blassberg, R.A., Felix, D.A., Tejada-Romero, B., and Aboobaker, A.A. (2013). PBX/extradenticle is required to re-establish axial structures and polarity during planarian regeneration. *Development* 140, 730–739.
- Blasse, C., Saalfeld, S., Etournay, R., Sagner, A., Eaton, S., and Myers, E.W. (2017). PreMosa: extracting 2D surfaces from 3D microscopy mosaics. *Bioinformatics* 33, 2563–2569.
- Burak, Y., and Shraiman, B.I. (2009). Order and stochastic dynamics in *Drosophila* planar cell polarity. *PLoS Comput. Biol.* 5, e1000628.
- Butler, M.T., and Wallingford, J.B. (2017). Planar cell polarity in development and disease. *Nat. Rev. Mol. Cell Biol.* 18, 375–388.
- Cebrià, F., and Newmark, P.A. (2005). Planarian homologs of netrin and netrin receptor are required for proper regeneration of the central nervous system and the maintenance of nervous system architecture. *Development* 132, 3691–3703.
- Chaikin, P.M., and Lubensky, T.C. (2000). *Principles of Condensed Matter Physics* (Cambridge University Press).
- Chen, C.C.G., Wang, I.E., and Reddien, P.W. (2013). pbx is required for pole and eye regeneration in planarians. *Development* 140, 719–729.
- Chien, Y.H., Keller, R., Kintner, C., and Shook, D.R. (2015). Mechanical strain determines the axis of planar polarity in ciliated epithelia. *Curr. Biol.* 25, 2774–2784.
- Chu, C.W., and Sokol, S.Y. (2016). Wnt proteins can direct planar cell polarity in vertebrate ectoderm. *eLife* 5, e16463.
- Dahmann, C., Oates, A.C., and Brand, M. (2011). Boundary formation and maintenance in tissue development. *Nat. Rev. Genet.* 12, 43–55.
- Frisch, D., and Farbman, A.I. (1968). Development of order during ciliogenesis. *Anat. Rec.* 162, 221–232.
- Glazer, A.M., Wilkinson, A.W., Backer, C.B., Lapan, S.W., Gutzman, J.H., Cheeseman, I.M., and Reddien, P.W. (2010). The Zn Finger protein Iguana impacts Hedgehog signaling by promoting ciliogenesis. *Dev. Biol.* 337, 148–156.
- Goodrich, L.V., and Strutt, D. (2011). Principles of planar polarity in animal development. *Development* 138, 1877–1892.
- Guirao, B., Meunier, A., Mortaud, S., Aguilar, A., Corsi, J.M., Strehl, L., Hirota, Y., Desoeuvre, A., Boutin, C., Han, Y.G., et al. (2010). Coupling between hydrodynamic forces and planar cell polarity orients mammalian motile cilia. *Nat. Cell Biol.* 12, 341–350.
- Gurley, K.A., Elliott, S.A., Simakov, O., Schmidt, H.A., Holstein, T.W., and Sánchez Alvarado, A.S. (2010). Expression of secreted Wnt pathway components reveals unexpected complexity of the planarian amputation response. *Dev. Biol.* 347, 24–39.
- Gurley, K.A., Rink, J.C., and Sánchez Alvarado, A.S. (2008). β -catenin defines head versus tail identity during planarian regeneration and homeostasis. *Science* 319, 323–327.
- Hale, R., and Strutt, D. (2015). Conservation of planar polarity pathway function Across the animal kingdom. *Annu. Rev. Genet.* 49, 529–551.
- Hazelwood, L.D., and Hancock, J.M. (2013). Functional modelling of planar cell polarity: an approach for identifying molecular function. *BMC Dev. Biol.* 13, 20.
- Herawati, E., Taniguchi, D., Kanoh, H., Tateishi, K., Ishihara, S., and Tsukita, S. (2016). Multiciliated cell basal bodies align in stereotypical patterns coordinated by the apical cytoskeleton. *J. Cell Biol.* 214, 571–586.
- Hoffmann, K.B., Voss-Böhme, A., Rink, J.C., and Brusch, L. (2017). A dynamically diluted alignment model reveals the impact of cell turnover on the plasticity of tissue polarity patterns. *J. R. Soc. Interface* 14, 20170466.
- Iglesias, M., Gomez-Skarmeta, J.L., Saló, E., and Adell, T. (2008). Silencing of Smed- catenin1 generates radial-like hypercephalized planarians. *Development* 135, 1215–1221.
- King, R.S., and Newmark, P.A. (2013). In situ hybridization protocol for enhanced detection of gene expression in the planarian Schmidtea mediterranea. *BMC Dev. Biol.* 13, 8.
- Klinger, E., Ricket, D., and Hasenauer, J. (2018). pyABC: distributed, likelihood-free inference. *Bioinformatics* 34, 3591–3593.
- Larsson, M., Gräslund, S., Yuan, L., Brundell, E., Uhlén, M., Höög, C., and Ståhl, S. (2000). High-throughput protein expression of cDNA products as a tool in functional genomics. *J. Biotechnol.* 80, 143–157.
- Lawrence, P.A., Struhl, G., and Casal, J. (2007). Planar cell polarity: one or two pathways? *Nat. Rev. Genet.* 8, 555–563.
- Lemullois, M., Boisvieux-Ulrich, E., Laine, M.C., Chailley, B., and Sandoz, D. (1988). Development and functions of the cytoskeleton during ciliogenesis in Metazoa. *Biol. Cell* 63, 195–208.
- Li, D.J., McMann, C.L., and Reddien, P.W. (2019). Nuclear receptor NR4A is required for patterning at the ends of the planarian anterior-posterior axis. *eLife* 8, e42015.
- Liu, S.Y., Selck, C., Friedrich, B., Lutz, R., Vila-Farré, M., Dahl, A., Brandl, H., Lakshmanaperumal, N., Henry, I., and Rink, J.C. (2013). Reactivating head re-growth in a regeneration-deficient planarian species. *Nature* 500, 81–84.
- Matis, M., and Axelrod, J.D. (2013). Regulation of PCP by the fat signaling pathway. *Genes Dev.* 27, 2207–2220.
- Merkel, M., Sagner, A., Gruber, F.S., Etournay, R., Blasse, C., Myers, E., Eaton, S., and Jülicher, F. (2014). The balance of prickle/spiny-legs isoforms controls the amount of coupling between core and Fat PCP systems. *Curr. Biol.* 24, 2111–2123.
- Meunier, A., and Azimzadeh, J. (2016). Multiciliated cells in animals. *Cold Spring Harb. Perspect. Biol.* 8, a028233.
- Mitchell, B., Jacobs, R., Li, J., Chien, S., and Kintner, C. (2007). A positive feedback mechanism governs the polarity and motion of motile cilia. *Nature* 447, 97–101.
- Mitchell, B., Stubbs, J.L., Huisman, F., Taborek, P., Yu, C., and Kintner, C. (2009). The PCP pathway instructs the planar orientation of ciliated cells in the *Xenopus* larval skin. *Curr. Biol.* 19, 924–929.
- Oderberg, I.M., Li, D.J., Scimone, M.L., Gaviño, M.A., and Reddien, P.W. (2017). Landmarks in existing tissue at wounds are utilized to generate pattern in regenerating tissue. *Curr. Biol.* 27, 733–742.
- Otsu, N. (1979). A threshold selection method from gray-level histograms. *IEEE Trans. Syst. Man Cybern.* 9, 62–66.
- Park, T.J., Mitchell, B.J., Abitua, P.B., Kintner, C., and Wallingford, J.B. (2008). Dishevelled controls apical docking and planar polarization of basal bodies in ciliated epithelial cells. *Nat. Genet.* 40, 871–879.
- Pearson, B.J., Eisenhofer, G.T., Gurley, K.A., Rink, J.C., Miller, D.E., and Sánchez Alvarado, A. (2009). Formaldehyde-based whole-mount in situ hybridization method for planarians. *Dev. Dynam.* 238, 443–450.
- Petersen, C.P., and Reddien, P.W. (2008). Smed- catenin-1 is required for anteroposterior blastema Polarity in Planarian Regeneration. *Science* 319, 327–330.
- Petersen, C.P., and Reddien, P.W. (2009). A wound-induced Wnt expression program controls planarian regeneration polarity. *Proc. Natl. Acad. Sci. U.S.A* 106, 17061–17066.
- Reddien, P.W. (2018). The cellular and molecular basis for planarian regeneration. *Cell* 175, 327–345.
- Reddien, P.W., Oviedo, N.J., Jennings, J.R., Jenkin, J.C., and Sánchez Alvarado, A.S. (2005). SMEDWI-2 is a piwi-like protein that regulates planarian stem cells. *Science* 310, 1327–1330.
- Reed, W., Avolio, J., and Satir, P. (1984). The cytoskeleton of the apical border of the lateral cells of freshwater mussel gill: structural integration of microtubule and actin filament-based organelles. *J. Cell Sci.* 68, 1–33.
- Reuter, H., März, M., Vogg, M.C., Eccles, D., Grífol-Boldú, L., Wehner, D., Owlarn, S., Adell, T., Weidinger, G., and Bartscherer, K. (2015). β -catenin-dependent control of positional information along the AP body axis in planarians involves a teashirt family member. *Cell Rep.* 10, 253–265.
- Rieger, R.M. (1981). Morphology of the Turbellaria at the ultrastructural level. *Hydrobiologia* 84, 213–229.
- Rink, J.C. (2018). Stem cells, patterning and regeneration in planarians: self-organization at the organismal scale. *Methods Mol. Biol.* 1774, 57–172.

- Rink, J.C., Gurley, K.A., Elliott, S.A., and Sánchez Alvarado, A. (2009). Planarian hh signaling regulates regeneration polarity and links hh pathway evolution to cilia. *Science* 326, 1406–1410.
- Rompolas, P., Azimzadeh, J., Marshall, W.F., and King, S.M. (2013). Analysis of ciliary assembly and function in planaria. *Methods Enzymol.* 525, 245–264.
- Rouhana, L., Weiss, J.A., Forsthöfel, D.J., Lee, H., King, R.S., Inoue, T., Shibata, N., Agata, K., and Newmark, P.A. (2013). RNA interference by feeding in vitro-synthesized double-stranded RNA to planarians: methodology and dynamics. *Dev. Dyn.* 242, 718–730.
- Rozanski, A., Moon, H., Brandl, H., Martín-Durán, J.M., Grohme, M.A., Hüttner, K., Bartscherer, K., Henry, I., and Rink, J.C. (2019). 3.0—Improvements to a mineable resource of flatworm biology and biodiversity. *Nucleic Acids Res.* 47, D812–D820.
- Sagner, A., Merkel, M., Aigouy, B., Gaebel, J., Brankatschk, M., Jülicher, F., and Eaton, S. (2012). Establishment of global patterns of planar polarity during growth of the *Drosophila* wing epithelium. *Curr. Biol.* 22, 1296–1301.
- Sánchez Alvarado, A., and Newmark, P.A. (1999). Double-stranded RNA specifically disrupts gene expression during planarian regeneration. *Proc. Natl. Acad. Sci. U.S.A.* 96, 5049–5054.
- Scimone, M.L., Cote, L.E., and Reddien, P.W. (2017). Orthogonal muscle fibres have different instructive roles in planarian regeneration. *Nature* 557, 623–628.
- Scimone, M.L., Lapan, S.W., and Reddien, P.W. (2014). A forkhead transcription factor is wound-induced at the planarian midline and required for anterior pole regeneration. *PLoS Genet.* 10, e1003999.
- Sonka, M., Hlavac, V., and Boyle, R. (2007). Image processing, analysis and machine vision (Thomson Engineering).
- Starruß, J., de Back, W., Brusch, L., and Deutsch, A. (2014). Morpheus: a user-friendly modeling environment for multiscale and multicellular systems biology. *Bioinformatics* 30, 1331–1332.
- Stückemann, T., Cleland, J.P., Werner, S., Vu, H.T.-K., Bayersdorf, R., Liu, S.-Y., Friedrich, B., Jülicher, F., and Rink, J.C. (2017). Antagonistic self-organizing patterning systems control maintenance and regeneration of the antero-posterior axis in planarians. *Dev. Cell* 40, 248–263.
- Szeliski, R. (2011). Computer vision (Springer).
- Taylor, J., Abramova, N., Charlton, J., and Adler, P.N. (1998). Van Gogh: a new *Drosophila* tissue polarity gene. *Genetics* 150, 199–210.
- Tu, K.C., Cheng, L.-C., T K Vu, H., Lange, J.J., McKinney, S.A., Seidel, C.W., and Sánchez Alvarado, A. (2015). Egr-5 is a post-mitotic regulator of planarian epidermal differentiation. *eLife* 4, e02238.
- van Wolfswinkel, J.C., Wagner, D.E., and Reddien, P.W. (2014). Single-cell analysis reveals functionally distinct classes within the planarian stem cell compartment. *Cell Stem Cell* 15, 326–339.
- Vásquez-Doorman, C., and Petersen, C.P. (2014). *zic-1* Expression in planarian neoblasts after injury controls anterior pole regeneration. *PLoS Genet.* 10, e1004452.
- Vinson, C.R., and Adler, P.N. (1987). Directional non-cell autonomy and the transmission of polarity information by the frizzled gene of *Drosophila*. *Nature* 329, 549–551.
- Vladar, E.K., Bayly, R.D., Sangoram, A.M., Scott, M.P., and Axelrod, J.D. (2012). Microtubules enable the planar cell polarity of airway cilia. *Curr. Biol.* 22, 2203–2212.
- Vogg, M.C., Owlarn, S., Pérez Rico, Y.A., Xie, J., Suzuki, Y., Gentile, L., Wu, W., and Bartscherer, K. (2014). Stem cell-dependent formation of a functional anterior regeneration pole in planarians requires Zic and Forkhead transcription factors. *Dev. Biol.* 390, 136–148.
- Wallingford, J.B. (2010). Planar cell polarity signaling, cilia and polarized ciliary beating. *Curr. Opin. Cell Biol.* 22, 597–604.
- Warrington, S.J., Strutt, H., Fisher, K.H., and Strutt, D. (2017). A dual function for prickle in regulating frizzled stability during feedback-dependent amplification of planar polarity. *Curr. Biol.* 27, 2784–2797.
- Werner, M.E., Hwang, P., Huisman, F., Taborek, P., Yu, C.C., and Mitchell, B.J. (2011). Actin and microtubules drive differential aspects of planar cell polarity in multiciliated cells. *J. Cell Biol.* 195, 19–26.
- Wong, L.L., and Adler, P.N. (1993). Tissue polarity genes of *Drosophila* regulate the subcellular location for prehair initiation in pupal wing cells. *J. Cell Biol.* 123, 209–221.
- Wu, J., Roman, A.C., Carvajal-Gonzalez, J.M., and Mlodzik, M. (2013). Wg and Wnt4 provide long-range directional input to planar cell polarity orientation in *Drosophila*. *Nat. Cell Biol.* 15, 1045–1055.
- Yang, J., Liu, X.Q., Yue, G.H., Adamian, M., Bulgakov, O., and Li, T.S. (2002). Rootletin, a novel coiled-coil protein, is a structural component of the ciliary rootlet. *J. Cell Biol.* 159, 431–440.
- Yang, Y., and Mlodzik, M. (2015). Wnt-frizzled/planar cell polarity signaling: cellular orientation by facing the wind (Wnt). *Annu. Rev. Cell Dev. Biol.* 31, 623–646.

STAR★METHODS

KEY RESOURCES TABLE

REAGENT or RESOURCE	SOURCE	IDENTIFIER
Antibodies		
Mouse monoclonal anti-Smed- ROOTLETIN-1 (clone PK2575-F08-2)	This paper	N/A
Rabbit polyclonal anti-Smed-CEP135	Azimzadeh et al., 2012	N/A
Mouse monoclonal anti-tubulin (clone DM1A)	Sigma-Aldrich	Cat#T6199-100µL; RRID:AB_477583
Goat anti-Mouse IgG (H+L) Cross-Adsorbed Secondary Antibody, Alexa Fluor 488	Thermo Fisher Scientific	Cat# A-11001; RRID:AB_2534069
Goat anti-Rabbit IgG (H+L) Cross-Adsorbed Secondary Antibody, Alexa Fluor 555	Thermo Fisher Scientific	Cat#A-21428; RRID:AB_2535849
Sheep polyclonal anti-Digoxigenin-POD, Fab fragments	Roche	Cat#11207733910; RRID: AB_514500
Sheep polyclonal anti-Fluorescein-POD, Fab fragments	Roche	Cat#11426346910; RRID: AB_840257
Sheep polyclonal anti-Digoxigenin-AP, Fab fragments	Roche	Cat#11093274910; RRID: AB_514497
Chemicals, Peptides, and Recombinant Proteins		
1,1,1-Trichloro-2-methyl-2-propanol hemihydrate or "Chloretoone"	Sigma-Aldrich	Cat#112054
Smed-ROOTLETIN-1	This study	N/A
Horse serum	Sigma-Aldrich	Cat# H1138
Roche Western Blocking Reagent	Sigma-Aldrich	Cat#11921673001
Trizol Reagent	Thermo Fisher Scientific	Cat#15596026
BCIP	Roche	Cat#11383221001
NBT	Roche	Cat#11383213001
Critical Commercial Assays		
Direct-zol™ RNA MiniPrep	Zymo Research	Cat#R2050
SuperScript III First-Strand Synthesis System	Thermo Fisher Scientific	Cat#18080051
SYBR™ Green PCR Master Mix	Thermo Fisher Scientific	Cat#4309155
Recombinant DNA		
pPRT4P vector	(Rink et al., 2009)	N/A
pAff8c vector	(Larsson et al., 2000)	N/A
pGEXK-M12 vector	MPI-CBG Protein Expression and Purification Facility	N/A
Deposited Data		
Accession number of genes used in this study are provided in Table S1	This study	N/A
Experimental Models: Organisms/Strains		
<i>Schmidtea mediterranea</i> asexual CIW4 strain	(Alvarado, 2002)	N/A
Oligonucleotides		
Primers for qPCR are provided in Table S1	This study	N/A
Primers for cloning are provided in Table S1	This study	N/A
Primers for dsRNA are provided in Table S1	This study	N/A
Software and Algorithms		
Fiji	ImageJ	https://fiji.sc
PreMosa image processing pipeline	(Blasse et al., 2017)	https://cblasse.github.io/premosa/usage.html

(Continued on next page)

Continued

REAGENT or RESOURCE	SOURCE	IDENTIFIER
GraphPad Prism	GraphPad Software	https://www.graphpad.com/scientific-software/prism/
Cilia polarity analysis algorithm	This study	Provide upon request
Simulation software Morpheus	(Starruß et al., 2014)	https://gitlab.com/morpheus.lab/morpheus

LEAD CONTACT AND MATERIALS AVAILABILITY

Further information and requests for resources and reagents should be directed to and will be fulfilled by the Lead Contact, Jochen Rink (rink@mpi-cbg.de). All unique and/or stable reagents and the custom code generated for this manuscript are available from the Lead Contact upon request.

EXPERIMENTAL MODEL AND SUBJECT DETAILS***Schmidtea mediterranea***

All experiments were performed on a clonal asexual strain of *Schmidtea mediterranea* (CIW4). All the animals were used in this study were of wild-type genotype and have indeterminate age because they are asexual. Animals were maintained at 20°C in 1× Monjuic salts (1.6 mmol/l NaCl, 1.0 mmol/l CaCl₂, 1.0 mmol/l MgSO₄, 0.1 mmol/l MgCl₂, 0.1 mmol/l KCl and 1.2 mmol/l NaHCO₃ prepared in Milli-Q water) (Cebrià and Newmark, 2005) and fed with calf liver once per week. Animals were starved for at least one week prior to experiments.

METHOD DETAILS**Cloning and RNA-Mediated Gene Silencing**

For gene cloning, DNA templates were amplified from cDNA using the primers in Table S1 and inserted into the pPR-T4P vector by ligation-independent cloning (Aslanidis and de Jong, 1990). RNAi of specific target genes was done by feeding liver paste mixed either with dsRNA-expressing *E. coli* (Sánchez Alvarado and Newmark, 1999) or in vitro synthesized dsRNA (Rouhana et al., 2013). RNAi feedings were performed with a two-day gap in between. β -catenin-1 and APC(RNAi) received 3 feedings, and all other knockdowns received 6 feedings.

Recombinant Protein and Antibody Production

The planarian ROOTLETIN-1 antibody was raised against a soluble fragment of the protein. Briefly, the fragment was identified via screening of 64 cDNA fragments resulting from the combinatorial use of 8 regularly spaced forward and reverse primers. Amplified fragments were cloned into the pGEX-M12 vector to add an N-terminal GST-tag, transformed into pRARE-expressing DH5alpha cells, induced with IPTG and the solubility of the specific fragments was assessed by ELISA of culture lysates using standard procedures. For antigen production, the most soluble fragment was retransformed into BL21 competent *E. coli* cells and expressed protein was purified over a glutathione matrix according to standard procedures (native purification). Monoclonal antibodies were generated at the MPI-CBG Antibody Facility as previously described (Stückemann et al., 2017).

Electron Microscopy

For ultrastructural analysis by electron microscopy, planarians were transferred into 200- μ m-deep flat carriers containing 20% BSA, and high-pressure frozen in an EMPACT2-RTS (Leica, Wetzlar, Germany) device. Frozen samples were freeze-substituted in a Leica AFS2 device at -90°C (40 h), followed by -30°C (8 h) in a cocktail containing 1% OsO₄, 0.1% uranyl acetate, 0.5% glutaraldehyde and 4% ddH₂O in acetone and brought to room temperature. The samples were washed in acetone, gradually infiltrated, and flat-embedded in epon-araldite resin. The resin was polymerized at 60°C over the weekend. Small pieces of embedded samples were remounted on a dummy resin block and 100-nm-thick sections were cut on a UCT (Leica) ultramicrotome and transferred to copper EM slot grids. The grids were stained for 10 min in 2% uranyl acetate in methanol followed by 2% lead citrate in H₂O for 5 min. Images were acquired on a Tecnai 12 (FEI, Eindhoven, The Netherlands) transmission electron microscope equipped with a 2k TVIPS (Gauting, Germany) camera.

Whole-Mount Antibody Staining

Planarians were anesthetized in cold 0.2% chloretone in planarian water until completely stretched out, positioned on a filter paper on a cold block with their ventral side up and killed/fixed with ice-cold MeOH for at least 1 hr at -20°C. The samples were then bleached in 6% H₂O₂ in MeOH overnight under direct light, gradually rehydrated to PBS with 0.1% Triton X-100 (PBSTx0.1%), transferred into reduction solution (1% NP40, 50mM DTT and 0.5% SDS in PBS) for 10 min at 37°C, followed by 2×10min washes with PBSTx0.1%.

The samples were then blocked for 1 hr in 10% filtered horse serum in PBSTx0.1%, followed by primary antibody incubation in blocking solution (anti-SMED-ROOTLETIN-1 1:500, and anti-SMED-CEP135 1:500) overnight at 4°C. The samples were washed 6–8 times for 4 hrs in PBSTx0.1%, and then incubated in secondary antibody in blocking solution (both secondary antibodies were used at 1:500) for 4 hrs at room temperature (or overnight at 4°C). Stained samples were washed 4–6 times for 2 hrs in PBSTx0.1%, and then mounted in 80% glycerol (prepared in 10mM Tris pH 8.5).

In Situ Hybridization

Whole-mount *in situ* hybridization was performed as previously described (King and Newmark, 2013; Pearson et al., 2009). For colorimetric development, samples were incubated in anti-DIG-AP (1:3000) in blocking solution (5% horse serum and 0.5% Roche Western Blocking Reagent in TNTx) overnight, and developed using NBT/BCIP. For fluorescent development, RNA probes of core PCP and Ft/Ds components were always developed first by incubating the samples in anti-DIG-POD (1:2000) in blocking solution and developed using tyramide amplification. Subsequently, RNA probe of epidermal marker *rootletin-1* was developed using anti-FL-POD (1:2000). Quenching of peroxidase enzyme was achieved by incubating samples in 100mM Sodium azide for >1 hr at RT. Following colorimetric development, animals were mounted in mounting media containing 75% glycerol and 2M urea.

qPCR

Total RNA from RNAi animals was extracted by mechanical homogenization in Trizol (Invitrogen, Paisley, UK) and purified using Direct-zol RNA MiniPrep kit (Zymo Research). cDNA was synthesized using SuperScript III reverse transcriptase (Invitrogen). qPCR was performed using SYBR Green PCR Master Mix (Applied Biosystems, Waltham, Massachusetts, United States of America). qPCR primer sequences are provided in [Table S1](#). Relative RNA abundance was calculated using the delta-Ct method after verification of primer amplification efficiency.

Light Microscopy and Image Analysis

All imaging was performed on a spinning disk Zeiss microscope equipped with a 40× Oil objective. Images were acquired as a tiled series of individual Z-stacks covering the entire ventral epidermis of the specimens. The resulting 3D image mosaic was processed using the image processing pipeline PreMosa (Blasse et al., 2017), which extracts the signal from the epidermal cells (on basis of the ROOTLETIN-1 and CEP135 channels) and tiles individual images. The PreMosa output is a 2D representation of the ventral epidermis, which was used as basis for all subsequent rootlet orientation analyses.

Details on the Model Equations

Two vector fields \vec{A} and \vec{M} are defined on a two-dimensional domain approximating the planarian body shape, rendering the precise value of \vec{A} and \vec{M} a function of the spatial position $\vec{x} = (x, y)$. These two fields represent two polarity components contributing independently to the observable ciliary rootlet polarity and are controlled by organizing regions at the head, tail and body margin.

For the geometric definition of the head, the tail and the body margin, we use the three static functions $H(x, y)$, $T(x, y)$ and $\vec{B}(x, y)$ that are markers for the head (red), the tail (blue) and the entire boundary (green curve in [Figure 4A](#)), respectively. H is set 1 where a head is located (at the anterior side in the wildtype) and 0 everywhere else. Analogously, T is set 1 where the tail is located (at the posterior side in the wild type) and 0 everywhere else. B is a vector of length 0 in the interior of the animal and of length 1 on the boundary pointing outwards and perpendicular to the boundary of the computation domain.

The spatiotemporal dynamics of \vec{A} and \vec{M} are given by two linear partial differential equations (PDE) in [Figure 4B](#). The operator \tilde{B} is defined here as $\tilde{B} \vec{Q} = (|B_x|Q_x, |B_y|Q_y)$ with $\vec{B} = (B_x, B_y)$ and $\vec{Q} = (Q_x, Q_y)$. The terms in these equations are motivated as follows. The first term (grey background) represents the action of the organizing regions at the head, the tail and the boundary. It generates nonzero values for \vec{A} and \vec{M} at certain locations at the boundary. For \vec{A} this happens at the head (encoded by H) and the tail (encoded by T). For \vec{M} this happens at the whole boundary (encoded by \vec{B}). The areas of H and T are chosen 5 lattice units wide, corresponding to 1% of the body length, and as long as 10% of the body width, as indicated by the colored areas in all simulation result figures. The term $\sim \alpha$ is a source term and the term $\sim \beta$ is a degradation term, both terms are only active on the respective boundary area. If no other terms in the PDE were present and the dynamics reached the steady state, \vec{A} would have magnitude α_H/β_H at H and point inwards ($\sim -\vec{B}$) and \vec{M} would have magnitude α_T/β_T at T and point outwards ($\sim +\vec{B}$). Similarly, if no other terms were present, \vec{M} would have magnitude α_B/β_B at the boundary \vec{B} and point outwards. Therefore, we can adjust the strength of the organizing regions at the boundary, the head and the tail by adjusting the α and the β parameters. In the presence of the other terms the values of \vec{A} and \vec{M} at the boundaries will change slightly since the described dynamics at the boundary is not equivalent to classic Dirichlet boundary conditions but allows us to model the dynamic adaptation of the boundary states in response to perturbed cues like the reduction of strength ($\sim \alpha$). Moreover, our dynamic and more flexible boundary effect can balance between boundary preference and bulk dynamics with few uniform parameters.

The second term (green background) represents degradation of the vector magnitude due to stochasticity and cell turnover, with subsystem-specific rates γ_A and γ_M . The third term (blue background) is a spatially averaging Laplacian with strength D_A and D_M representing the neighbor-neighbor coupling as used previously in continuum models of fly wing polarity (Merkel et al., 2014). The

Laplacian acts component-wise on the vectors. Numerically, a square lattice and no flux boundary conditions around the body margin are used.

To obtain the polarity field \vec{P} , the two fields \vec{A} and \vec{M} are superimposed on each other by a simple linear combination and then normalized to modulus 1 for non-vanishing superposition. The parameters δ_A and δ_M represent the responsiveness of the cells to the \vec{A} and \vec{M} fields. These parameters range from 0 to 1 where 1 represents complete responsiveness and 0 complete unresponsiveness.

Simulation Details

The equations were simulated using Morpheus (Starruß et al., 2014). The simulations were performed on a domain having an approximate planarian body shape on a 160×50 grid with $\Delta x = 0.5$. A forward Euler method with $\Delta t = 0.05$ was used for integrating the equations. Except for the *pbx(RNAi)* and the *pbx/ds(RNAi)* simulations, the equations were integrated until steady-state was reached.

Parameter Estimation

Control Condition

For the wild type in the model, we set δ_A and δ_M to 1, representing complete responsiveness to the polarity components \vec{A} and \vec{M} and fit the other parameter values as follows. The approximately linear decrease of splay along the A/P axis indicates that the degradation terms are small and that D_A is large but D_M is relatively smaller. Because the strengths of the head, tail and boundary organizing regions are set by the respective ratios α/β , we fix all β parameters to 1.0 and search for values of the α parameters that match the experimentally measured splay profile. Again, this task is made easier by the gradual change in splay along the A/P axis. By symmetry, in the A/P-center of the animal the x projection of \vec{P} equals \vec{A} and the y projection equals \vec{M} . Hence, in the center of the animal the tangent of the splay angle equals $\frac{|\vec{M}|}{|\vec{A}|} \sim \frac{2\alpha_B}{\alpha_H + \alpha_T}$. Analogously, similar relations can be found at other positions of the animal. Inserting

experimentally measured splay angles thereby yielded prior information for the distributions of the α parameters. Then, using an iterative solver directly for the steady state problem in the realistic domain geometry and pyABC (Klinger et al., 2018) as a Bayesian framework with the above priors and the average angle mismatch between experiment and model over all grid nodes as the summary statistics, we obtained candidate parameter combinations. The average error was 17 degrees angle mismatch per grid node. The parameter combinations were tested in time course simulations using Morpheus (Starruß et al., 2014) for robustness of the final splay profile to small changes of parameter values (Figure S4A). All parameter choices are shown in Table S2.

β -catenin-1(RNAi) and APC(RNAi)

The parameter values for simulating the β -catenin-1(RNAi) and APC(RNAi) cases are exactly the same as for the Control. The only differences for the simulations are the T and H functions. For β -catenin-1(RNAi) we set $T^{bcat} = 0$ everywhere (there is no tail present) and $H^{bcat} = H^{ctrl} + T^{ctrl}$ (there is another head where the tail was before). Similarly, we set $H^{apc} = 0$ everywhere (there is no head present) and $T^{apc} = H^{ctrl} + T^{ctrl}$ (there is another tail where the head was before). Figures 4D and 4E show simulation results that match the observed polarity fields. Moreover, we tracked the position of the repolarization front $x_F(t)$ in such a time-course simulation for β -catenin-1(RNAi) with the parameter values of the Control condition, see Video S1, and compared it to the measured front trajectory in Figure 4I. To obtain $x_F(t)$, we averaged the vector field \vec{P} over all M/L points with identical A/P position and recorded the front position $x_F(t)$ where this laterally averaged A/P dependency switches from posterior-ward (0 degrees) to anterior-ward (180 degrees). The qualitative shape of this theoretical prediction $x_F(t)$ matched the experimental data very well, without adjusting any model parameter. Further, the time unit of all model parameters, which does not affect the steady state patterns evaluated in other figures, was universally set to 1 h. This single parameter choice was sufficient to reproduce two characteristic time scales of the experimentally measured data: the initial lag of 3 days and the slowing down of the front speed, which further supports the model assumptions.

Remaining RNAi Experiments

The molecular details of the *pbx(RNAi)* experiments suggests inactivated head and tail organizers, that means we should have $\alpha_T^{Pbx} = \alpha_H^{Pbx} = 0$. This however, would mean that the A/P polarity component completely disappears, which is not what we observe. Therefore, we simulate the *pbx(RNAi)* condition by starting with the Control steady-state, switch off head and tail by setting $\alpha_T^{Pbx} = \alpha_H^{Pbx} = 0$ and assume that the observed polarity pattern upon *pbx(RNAi)* corresponds to a transient state at a certain time t when the A/P field \vec{A} has not yet completely decayed. In the simulations we used $t = 2.5$. In this case a very good fit to the observations is achieved (Figure 4F and S4B).

All following simulations are carried out until the steady state is reached. For most of the remaining RNAi experiments all parameters are taken unchanged from the Control case and only the δ_A and δ_M parameters are adjusted. In the *ds(RNAi)* and *ft-1,-2(RNAi)* conditions, smaller splay is observed than in the Control, therefore we fix $\delta_A = 1$ for both cases and manually adjust δ_M until the splay in the simulations is close to the experiments. As a result, we find $\delta_M^{Ds} = 0.5$ and $\delta_M^{Ft} = 0.6$. This model fit with a reduced role of the \vec{M} component agrees with the putative role of Ds and Ft in propagating the M/L cue from the body margin. For the results see Figures S4C and S4D.

The *pbx/ds* double RNAi condition is simulated by simply combining the *pbx(RNAi)* parameters with the *ds(RNAi)* parameters and not fitting any parameter. This means we again determine the fields \vec{A} and \vec{M} at a time $t = 2.5$ after inactivating head and tail and use $\delta_M^{Pbx-Ds} = \delta_M^{Ds} = 0.5$. With these parameters a very good agreement is found between experiments and simulations (Figure S4E).

We proceed similarly for the *vang-1,-2(RNAi)* conditions. As in these animals, larger splay is observed than in the Control we fix $\delta_M = 1$ and find by manual fitting $\delta_A^{Vangs} = 0.7$, in agreement with a role for Vangs in propagating the A/P cue from the head and tail (Figure S4F). Note, this result is not reproducible with a simpler one-component model except by a technical work-around of decreasing both A/P sources or increasing the M/L source that are not supported by the role of Vangs.

For the Dvl case this procedure of reducing δ_A^{Dvl} does not result in satisfying fits. The splay is either too large in the anterior region or too small in the posterior region. However, the situation changes after we switch off the tail organizer by setting $\alpha_T^{Dvl} = 0$, which agrees with a dual role for Dvls in core PCP propagating the A/P cue and in tail specification. With the inactivated tail, $\delta_A^{Dvl} = 0.7$ yields a good fit to the observed splay profile (Figure S4G), keeping the \vec{M} field unperturbed ($\delta_M = 1$). Note, if we reduce the cell-cell coupling strength D_A as motivated by a possible role of Dvl in Frz-Stbm transcellular complex formation, then splay approaches 90 degrees away from the anterior and posterior poles. While the reduction of D_A alone does not reproduce the experimentally observed splay profile (about 65 degrees in the trunk region) as accurate as the above parameter set, a moderate D_A reduction could complement the above parameter set and yield a similar model result (data not shown). Importantly, combining the settings for *dvl-1,-2(RNAi)* and *ds(RNAi)* provides the parameters for the *dvl-1,-2/ds* triple RNAi condition, i.e. $\delta_M^{Dvl-Ds} = \delta_M^{Ds} = 0.5$, $\delta_A^{Dvl-Ds} = \delta_A^{Dvl} = 0.7$ and $\alpha_T^{Dvl-Ds} = \alpha_T^{Dvl} = 0$. This fit-free model prediction of the triple RNAi condition matches well with the observed splay profile (Figure S4H).

QUANTIFICATION AND STATISTICAL ANALYSIS

Rootlet Detection and Orientation Quantification

For rootlet detection, the rootlet signal was first reduced to present its major axis by applying a Difference-of-Gaussian filter ($\sigma_1 = 0.5$, $\sigma_2 = 5$) (Sonka et al., 2007). To segment the rootlets in the enhanced images, an adaptive thresholding approach was applied using a local threshold being determined by the Otsu method (Otsu, 1979). To remove false positives or unresolved clusters of ciliary rootlets, connected components that do not fit the expected size of a ciliary rootlet (8–10 pixels under our imaging conditions) were filtered out. The same approach was applied for segmenting the basal bodies.

To obtain the rootlet orientation, an ellipse was fitted to each detected component. The orientation and length of the major and minor axes are given by the eigenvectors and eigenvalues of the resulting covariance matrix. All detected components with major axes (eigenvector of the largest eigenvalue) < 2 than the minor axis (eigenvector of the second largest eigenvalue) were filtered out, since orientation can only be meaningfully determined for elongated ROOTLETIN-1 positive structures. For all remaining rootlets, the largest eigenvector presents the major axis and, thus, orientation. To determine the sign of the orientation within the interval $[0^\circ, 360^\circ]$, the asymmetric position of the CEP135-positive basal body at the base of the rootlet was used. Unique assignments of the closest basal body to each ciliary rootlet were made using a formulation of a bipartite matching problem. Since polarities comprise a directed orientation within the interval $[0^\circ, 360^\circ]$, it is still necessary to determine the correct sign of the estimated orientation. From the literature, it is known, that the basal body appears at the base of the rootlets, thus the position of the basal bodies allows the determination of the unknown directionality. We utilize a formulation of a bipartite matching problem to uniquely assign the closest basal body to each ciliary rootlet. Let R be the set of ciliary rootlets and B the set of basal bodies, then a matching $m = (V, E)$ can be defined as a weighted bipartite graph with:

$$V = R \cup B \quad E = R \times B$$

$$\text{with } \forall e_{ij} \in E \quad c(e_{ij}) = \begin{cases} d(R_i, B_j) & d(R_i, B_j) \leq 5 \\ \infty & \text{otherwise} \end{cases}$$

For each edge $e_{ij} \in E$, the cost $c(e_{ij})$ is defined as the Euclidean distance between the center of the basal body B_j and the closest tip of the rootlet R_i . To reduce the size of the matching problem and to prevent implausible assignments, only edges with a distance less or equal than 5 are considered. Using a greedy algorithm to compute a matching reveals a solution that locally minimizes the total costs of used edges and rather leaves a rootlet or basal body unmatched than assigning them to the wrong matching partner. Even if this does not obtain a global optimal solution, the majority of basal bodies are correctly matched. For each ciliary rootlet, the solution reveals either an exclusion from the analysis, if no reasonable assignment could be determined, or a unique basal body that localizes near one of its tips. The position of a matched basal body finally enables the determination of a direction of the previously estimated rootlet orientation. With that, it is possible to assign a polarity $p = P(\theta) \in \{1, \dots, 8\}$ to the ciliary rootlet being elongated and having a basal body near its tip.

To infer the polarity for entire cells or tissues, a cell segmentation is required, which yields the area of each cell within the epithelium. Since it was not possible to visualize cell membranes uniformly in our immunostaining protocol, the cell segmentation is determined from a Voronoi tessellation having the cell nuclei as starting points. To detect all cell nuclei in the 2D image, we apply the Fiji plugin *Descriptor-based Registration (2D/3D)* (Szeliski, 2011). This plugin is a tool to register two images by matching two-point clouds whereby the used points are identified by a Difference-of-Gaussian detector accepting only blob-like structures of a predefined size. Although it is designed to register two images, we exploit it to detect cell nuclei, which also yield roundish structures of a specific

size. The detected positions serve as starting points to partition the image into polygons using a Voronoi diagram (Blasse et al., 2017). Since we could observe, that the cell nuclei locate exactly in the center of the cell, the Voronoi tessellation is a reasonable approach to estimate the cell boundaries.

To summarize the rootlet polarities of each cell being expressed by both an angle $\theta \in [0^\circ, 360^\circ]$ and a polarity $p = P(\theta) \in \{1, \dots, 8\}$, we determine the cell polarity p_C via majority voting:

$$p_C = \operatorname{argmax}_p \left\{ \sum_{i=1}^N 1 | V_{p \in \{1, \dots, 8\}} : p_i = p \right\}$$

The analysis revealed that each cell features on average 30 rootlets. Thus, if a cell deviates significantly from that, then there must be a mistake in the cell segmentation clustering or splitting correct cells. To exclude these cells from the analysis, we reject cells featuring less or more than the allowed rootlet number. Currently, we accept cells having 10–70 rootlets. All remaining cells feature a reasonable rootlet number, which is summarized to a common cell polarity.

Mathematical Methods for Ciliary Rootlet Statistics

Data of individual ciliary rootlet angles were treated as normal vectors and averaged within boxes of a 150×150 pixel grid, approximately representing the area of one to two cells under our imaging conditions. The resulting average vector per box was normalized to unit length. Data from cilia close to the tissue border and the pharynx were excluded. The resulting vector maps were used for all statistical analyses (Figures 2D–2H, 3C, 3F, 3I, 4H, 5D, 5H, 6E, 6G, 6J, S2B, S2C, S2E, S2F, S3B, S3C, S4A–S4H, S4M, S5E–S5G, S5J, S6E, and S7C). The chosen statistical tests and sample numbers n are given in the corresponding figure captions. For visualization of vector maps in the figures (Figures 2C, 3B, 3E, 3H, 5C, 5G, 6D, S3D, S4J–S4L, S5K, S6F, and S7B), coarser grids were used in order to obtain a visible vector size and density across different animal sizes (grid size was adjusted to specimen size). Graphs quantifying the splay of rootlet vectors against the A/P axis were calculated by averaging vectors along stripes in horizontal or vertical directions using a coordinate system that was aligned to the long and short main axes of each individual animal, i.e. the best-fitting ellipsoid to its shape, and scaling position by axis length resulting in relative position values from 0 to 1. For the quantification of splay angles, we extracted average rootlet orientation along straight, midline-orthogonal contours from the left to the right body margins. The average splay angle change at a given A/P axis position was defined by a linear fit to the slope of the resulting transverse orientation profile (illustrated in Figures 2F–2H). Since animal widths (and lengths) were scaled to 1, the calculated slope of the splay angle fit also approximates the total splay angle difference between the left and right margins. The trajectories displaying the change of the splay angle all along the A/P axis (e.g., Figures 5D, 5E, S5G, S5H, 6E–6H, 6J, and 6K) were generated via a systematic repetition of the above splay angle change quantifications along the A/P axis. Custom C-code was used for the above statistical analysis and is available upon request from the Lead Contact.

DATA AND CODE AVAILABILITY

Sequences of unpublished genes used in this study were deposited in GenBank: MH253608-17.

The authors declare that the data supporting the findings of this study and custom code generated for the manuscript are available from the Lead Contact, Jochen Rink (rink@mpi-cbg.de), upon request.